Open access • Journal Article • DOI:10.1142/S021820251100543X

Particle simulations of morphogenesis — Source link

Petros Koumoutsakos, Basil Bayati, Florian Milde, Gerardo Tauriello

Institutions: ETH Zurich

Published on: 24 Oct 2011 - Mathematical Models and Methods in Applied Sciences (World Scientific Publishing Company)

Particle simulations of morphogenesis

Koumoutsakos, P ; Bayati, B ; Milde, F ; Tauriello, G

Abstract: The simulation of the creation and evolution of biological forms requires the development of computational methods that are capable of resolving their hierarchical, spatial and temporal complexity. Computations based on interacting particles, provide a unique computational tool for discrete and continuous descriptions of morphogenesis of systems ranging from the molecular to the organismal level. The capabilities of particle methods hinge on the simplicity of their formulation which enables the formulation of a unifying computational framework encompassing deterministic and stochastic models. In this paper, we discuss recent advances in particle methods for the simulation of biological systems at the mesoscopic and the macroscale level. We present results from applications of particle methods including reaction diffusion on deforming surfaces, deterministic and stochastic descriptions of tumor growth and angiogenesis and discuss successes and challenges of this approach.

DOI: https://doi.org/10.1142/S021820251100543X

World Scientific
www.worldscientific.com

PARTICLE SIMULATIONS OF MORPHOGENESIS

PETROS KOUMOUTSAKOS*, BASIL BAYATI, FLORIAN MILDE
and GERARDO TAURIELLO

Institute of Computational Science,
ETH Zurich, CH-8092, Switzerland
**petros@ethz.ch*

Received 19 January 2011
Communicated by N. Bellonio and F. Brezzi

The simulation of the creation and evolution of biological forms requires the development of computational methods that are capable of resolving their hierarchical, spatial and temporal complexity. Computations based on interacting particles, provide a unique computational tool for discrete and continuous descriptions of morphogenesis of systems ranging from the molecular to the organismal level. The capabilities of particle methods hinge on the simplicity of their formulation which enables the formulation of a unifying computational framework encompassing deterministic and stochastic models. In this paper, we discuss recent advances in particle methods for the simulation of biological systems at the mesoscopic and the macroscale level. We present results from applications of particle methods including reaction diffusion on deforming surfaces, deterministic and stochastic descriptions of tumor growth and angiogenesis and discuss successes and challenges of this approach.

Keywords: Particle methods; morphogenesis; reaction−diffusion; tumor growth; vasculogenesis.

AMS Subject Classification: 74E99, 74E92

1. Introduction

Morphogenesis, (*morphi+ genesis*, the Greek words for form and creation) is a fundamental process that governs biological systems from the time of their creation to the time of their death. The name is perhaps tribute to ancient Greek thinkers, like Aristotle, who first contemplated about the "potential" of simpler biological structures, such as the egg, to contain the blueprint and the interaction rules that lead to the development of complex living organisms. As shape is intrinsically linked with our perception capabilities, morphogenesis is usually understood in terms of the visible structures such as tissues' organs and organisms. The advent of modern imaging tools enables us to probe the interactions of molecules and the assembly of macromolecular complexes and intricate mechanisms of cell division and proliferation thus extending the notion of morphogenesis from the molecular to the organismal level.

One of the main underlying principles of morphogenesis for biological systems at different scales in space and time is the interaction between components that have a certain potential to interact. The key concepts of biological morphogenesis as described by Davies[43] are molecular mechanisms that initiate and control shape, the principle of emergence of complex structures and behaviors from the interactions of comparatively simpler components, the use of feedback, self-assembly and adaptive self-organization. One can readily recognize that many of the concepts that are critical to morphogenesis are also relevant to other natural processes and to humans creations. They have been the subject of intense investigations in physics, chemistry and engineering. Examples range from (biomorphic) crystals,[60] to sand-dunes[15] and cities.[74]

The study of morphogenesis by physicists and mathematicians is often subjected to simplifications, as scientists wish to identify its key components so that they can in turn be analyzed and understood. This idealization and simplification appears at times to not be commensurate with the complexity of biological systems but it is a well-established method of scientific inquiry. The pioneering work of D'Arcy Thompson on Growth and Form,[152] proposed a mathematical formalism for the description of biological forms and proposed a number of mechanisms for growth. Among those, spatially dependent chemical reactions and diffusive processes figure prominently as one of the mechanisms that determine the growth and structural characteristics of several organisms. A few years later, Turing[154] proposed reaction−diffusion models that depend on local autocatalysis and long-range inhibition to explain a wide range of phenomena related to biological pattern formation. The work of Turing has been the starting point for mathematical and computational studies of morphogenesis with a marked increase in attention to the subject in the last two decades. Among the various mathematical models of morphogenesis,[151,112] there has been particular emphasis on the reaction−diffusion process that lead to patterning[85,96,157] as the distribution of chemicals on a surface may have an influence on its subsequent evolution, with examples ranging from tumor[48,35,127,95,58,109] to animal and plant growth.[77,82,16] Simulations of reaction−diffusion processes have often implemented techniques such as finite elements that rely on a proper triangulation of the geometry[72] a procedure that may become cumbersome when the surface topology exhibits large variations and break-ups. The development of level sets[110] has opened new frontiers in simulating evolving surfaces as they can accommodate large deformations and break-ups. The extension of level sets to solving partial differential equations on surfaces[29] has led the development of methods to handle the transport of surface bound substances on deforming surfaces.[160,5,133] Reaction−diffusion models are usually formulated either in terms of deterministic rate equations or by using stochastic descriptions of the underlying molecular processes. The stochastic description provides detailed information about the dynamics of the reaction−diffusion process, albeit at a significant computational cost over deterministic simulations. The Stochastic Simulation Algorithm, Sec. 5, (SSA)[64,65] has been used extensively in biochemical modeling (Refs. 153, 88 and references therein) of

March 15, 2011 6:53:55pm WSPC/103-M3AS 00543 ISSN: 0218-2025 1st Reading

reactions that assume a homogeneous spatial distribution of the species involved. A number of algorithms[66,63,13] have been presented for the acceleration of the SSA for homogeneous systems. In recent years, the SSA has been extended to simulations involving spatially inhomogeneous molecular distributions undergoing diffusion and reaction processes.[51,73,126] The algorithm presented in Refs. 51 and 73 scales almost linearly with the number of events, but requires them to be scheduled thus prohibiting parallel execution. In Ref. 126 the computational time is reduced by splitting the reaction−diffusion phenomena into two distinct diffusion and reaction phases. This splitting may introduce numerical artifacts for systems close to a microscopic level as the reaction and diffusion processes happen concurrently, in particular for systems that involve too few particles to be insensitive to this kind of splitting. Recent works have examined the qualitative behavior of stochastic systems and have provided extensions for the deterministic systems to include leading order corrections for molecular noise,[140,147] hence losing some of the descriptive benefits of a completely stochastic simulation but with the advantage of a relative reduction in computational cost. A number of issues remain open in spatial SSA, such as the modeling of the diffusion rates in complex geometries, algorithms of increased computational efficiency and accuracy, and the enforcement of the homogeneity assumption.[88]

Besides reaction−diffusion models, there has been an ever increasing interest in constructing models of morphogenesis that are multiscale thus reflecting the very essence of this process (see Refs. 23, 24 and references therein). It is evident[52] that differential signaling alone is not sufficient to help us model the plethora of forms and functions. Computational models that take into account as well mechanical,[70] and genetic processes and their interactions are necessary. The effective simulation Morphogenesis requires a multiscale and multi-disciplinary approach. The phenomena that are involved in Morphogenesis (as well as in many other biological processes) can be found in a number of other problems and a number of effective computational techniques have been proposed in order for example to simulate mechanics, fluids or biochemistry. What is different here is that these different processes interact in a truly multiscale fashion and it is necessary to take these interactions into account when devising computational methods to study morphogenesis. Recent efforts in developing a framework for the simulation of morphogenesis[38] have provided us with effective tools to address a multitude of biological problems. These tools rely on the simplicity of the individual components and rely on developing modeling assumptions that can be translated into interactions of the individual components.

This description matches very well, the topic of this paper, which is the use of particle methods for Computational Morphogenesis. Particle methods rely on tracking their locations ($\mathbf{r}$) and the evolution of their properties ($Q(t)$) based on interaction rules that reflect the physics that is being simulated. Particle methods may be broadly described as solving Newtons equations

$$\frac{d^2 r_i}{dt^2} = \mathbf{F}(r_i, r_j, Q_i, Q_j, \ldots), \tag{1.1}$$

where the force field **F** can be obtained either by a divergence of stress−tensor or as the gradient of a potential. Hence all modeling aspects of particle methods are concentrated on the right-hand side while a common computational framework can be constructed to account efficiently for particle tracking and their interactions. Particle methods were the first method used to describe the simulation of physical processes (in the 1930's hand made calculations by Rosenhead of the evolution of a vortex sheet[128]) and they have been advocated for efficient simulations of multiphysics phenomena in complex deforming computational domains in several fields of science ranging from astrophysics to fluid and solid mechanics (see the review papers[93,86,103] and references therein). Particle simulations of morphogenesis have been first reported in the graphics community and were in fact among the first methods used to simulate phenomena such as plant growth.[83,144] Particle methods are unique, in that they can be used to simulate phenomena ranging from the atomistic scale (as in Molecular Dynamics) to the mesoscale (as in kinetic models of complex physics) and the macroscale (as in fluid, solid mechanics and astrophysics). In addition, they can be readily formulated to describe discrete and continuous processes as well as deterministic and stochastic models. In recent years starting from the development of particle methods for the simulation of three-dimensional vortical flows,[90] these techniques have been extending to the simulation of continuous processes biological systems, such as diffusion in cell organelles[137,136] to more recent work in simulations of angiogenesis[101] and on reaction−diffusion equations on deforming surfaces.[27] The various types of models of angiogenesis, are representative of the models used in morphogenesis and they can be classified in three broad categories:

(1) Discrete, cell-based models that aim to capture the behavior of individual biological cells,[17]
(2) Continuum models that describe the large scale, averaged behavior of cell populations[10,91]
(3) Discrete models that model explicitly vascular networks determined by the migration of tip cells.[34,148]

Besides angiogenesis, a number of computational models capturing cell−cell interactions for the simulation of tissue formation have been introduced over the years.[11,108,79] Cell-based models define single cells as distinct entities and are well-suited to model small populations of heterogenous cellular systems. The cellular granularity of the models allows for the integration of cell−cell interactions such as cell−cell signaling, cell−cell adhesion and the cell cycle. Limitations of these models are associated with the high computational cost for simulating systems of large number of cells. In the realm of cell-based modeling, we can distinguish grid-based and particle-based models. Grid-based models include the Cellular Automata (CA)[9] where each cell is represented by a single grid element. An extension to this model is the Cellular Potts model (CPM) where single cells are discretized as a collection of grid elements.[67] Finite Element Models (FEM) have been considered to model the

March 15, 2011 6:53:56pm WSPC/103-M3AS 00543 ISSN: 0218-2025 1st Reading

mechanical properties of single cells[98] and of plant cell walls under pressure.[145] A hybrid Mass-Spring/FEM model for plant tissues has been proposed in Ref. 62.

In particle-based models, cells are modeled as soft spherical objects that interact via potential forces[49] and are governed by interparticle deterministic and stochastic dynamics. Cell shape changes are induced by cell adhesion and compression. To account for the cell shape changes during mitosis, Byrne and Drasdo[31] introduced dumb-bell shaped cells and Palsson *et al.*[113] introduced an elliptical model to account for elongated cell shapes during migration. The Subcellular Element Model (SEM) was proposed[8,107,135] to describe tissues with individually deformable cells represented by a collection of particles. These subcellular elements interact with each other through soft breakable-bond potentials. Model simulations are governed by Brownian dynamics. Christley *et al.* have presented a GPU implementation of the SEM and provided general guidelines to follow when considering a GPU accelerated implementation of cell-based computational models.[37] Jamali *et al.* introduced a subcellular viscoelastic model that defines cell-internal, cell−cell and cell-environment interactions via bound Kelvin−Voigt subunits. A cell is composed of subcellular elements representing the plasma membrane, the cytoskeleton and the nucleus.[79] Liedekerke *et al.* proposed a hybrid method that combines smoothed particle hydrodynamics (SPH) to model the liquid phase inside a cell with a discrete element method (DEM) to model the solid, elastic phase of the cell walls. The model further considers the transport of water through the semipermeable cell wall.[156] Dissipative Particle Dynamics (DPD) are another class of particle based models and have been used to model red blood cells[118] and recently to explain the stress distribution in cell tissue experiencing cell division and apoptosis.[122] The Immersed Boundary Method (IBM) for cells presented by Rejniak *et al.*[124,125] combines an elastic representation of the cell membrane modeled as a collection of massless springs, with a viscous incompressible fluid as described by the Navier−Stokes equation, to represent the cell cytoplasm and the extracellular matrix.

We wish to emphasize that the papers listed here pertain to morphogenesis and they do not constitute an exhaustive (or even representative) list of the vast literature on the subject of particle methods.

The present paper is organized as follows: In Sec. 2, we present the fundamentals of particle methods for the solution of convection-diffusion reaction equations. We remain in the continuum realm in Sec. 3 to describe the evolution of surfaces and along with the solution of partial differential equations on them. In Sec. 4, we present applications of these methodologies as they pertain to pattern formation, avascular tumor growth and angiogenesis. The details of the components of the biological models are presented so as to provide a comparatively complete description of the capabilities of particle methods. In Sec. 5, we present stochastic particle methods for the solution of reaction diffusion equations with applications on pattern formation and glioma growth. The last Sec. 6 outlines particle models for cells that carry the potential for a bottom up description of morphogenesis. We conclude with a summary of our findings and with directions for future work.

2. Particle Methods

Particle methods can be used to simulate systems ranging from water transport in nanotubes to galaxy formation. This unique property of particle methods relies on the formulation of physical systems as interactions between evolving particles. This common algorithmic framework can be used to describe discrete and continuum systems. Particle methods for continuum systems, such as Smoothed Particle Hydrodynamics, Vortex Methods, and Lagrangian Level Sets, are based on the Lagrangian formulation of the governing equations, the formulation of the governing equations as integral equations and in turn the use of particles as quadrature points for their discretization. Particles interact and adapt according to a convection velocity field but the non-uniform distortion of the computational elements prevents the convergence of the method. Hence particles evolve while conserving moments of the field they aim to discretize, albeit inconsistently with the equations that govern their evolution. This observation is often overlooked in simulations using particles but we consider that particle distortion and the ensuing inaccuracy of the method are inherently linked to the Lagrangian description of particle methods. In order to correct for this inaccuracy of continuous particle methods, a number of regularization procedures have been proposed, that can be distinguished as weight or location processing. Here we discuss the process of particle regularization by remeshing the particles periodically on grid nodes. Remeshing detracts from the grid free character of particles but enables advances such as multiresolution, the coupling continuum and atomistic descriptions and last but not least the development of software that seamlessly simulates systems across several scales.

2.1. *Functions described by smooth particles*

Point particle approximations were the first to attract attention in solving fluid mechanics problems because their evolution can be formulated in terms of conservation laws. An approximation of a smooth function f in the sense of measures[123] can be formulated as:

$$f^h(\hat{\mathbf{x}}) = \sum_p w_p \delta(\mathbf{x} - \mathbf{x}_p),$$

where w_p denotes the weights of the particles and depends on the quadrature applied to discretize on Eq. (2.1). The point particle approximations need to be enhanced in order to recover continuous fields (see Ref. 40 and references therein). Continuous fields can be recovered from point samples by regularizing their support, replacing δ by a smooth *cutoff* function that obeys the partition of unity and has a compact support:

$$\delta(\mathbf{x}) \simeq \zeta_\epsilon(\mathbf{x}) = \epsilon^{-d} \zeta\Big(\frac{\mathbf{x}}{\epsilon}\Big), \tag{2.1}$$

where d is the dimension of the computational space and $\epsilon \ll 1$ is the range of the cutoff.

March 15, 2011 6:53:57pm WSPC/103-M3AS 00543 ISSN: 0218-2025 1st Reading

Smooth function approximations can be constructed by using a mollification kernel $\zeta_\epsilon(\hat{\mathbf{x}})$:

$$f_\epsilon(\hat{\mathbf{x}}) = f \star \zeta = \int f(\mathbf{y})\zeta_\epsilon(\hat{\mathbf{x}} - \mathbf{y})\, d\mathbf{y}.$$

The particle approximation of the regularized function is defined as

$$f_\epsilon^h(\hat{\mathbf{x}}) = f^h \star \zeta_\epsilon = \sum_p w_p \zeta_\epsilon(\hat{\mathbf{x}} - \hat{\mathbf{x}}_p). \tag{2.2}$$

The error introduced by the quadrature of the mollified approximation f_ϵ^h for the function f can be distinguished in two parts as:

$$f - f_\epsilon^h = (f - f \star \zeta_\epsilon) + (f - f^h) \star \zeta_\epsilon. \tag{2.3}$$

The first term in Eq. (2.3) denotes the mollification error that can be controlled by appropriately selecting the kernel properties. The second term denotes the quadrature error due to the approximation of the integral on the particle locations. Since the early 1980s, mollifier kernels have been developed in VMs with an emphasis on the property of moment conservation to comply with vorticity moments conserved by the Euler equations. The accuracy of these methods is related to the moments that are being conserved, and a method is of order r when:

$$\begin{cases} \int \zeta(\hat{\mathbf{x}})\, d\hat{\mathbf{x}} = 1, \\ \int \mathbf{x}^{\mathbf{i}} \zeta(\hat{\mathbf{x}})\, d\hat{\mathbf{x}} = 0 \qquad \text{if } |\mathbf{i}| \leq r - 1 \\ \int |\hat{\mathbf{x}}|^r, |\zeta(\mathbf{x})|\, d\mathbf{x} < \infty. \end{cases}$$

The overall accuracy of the method is then, for smooth functions f:

$$\|f - f_\epsilon^h\|_{0,p} \sim \mathcal{O}(\epsilon^r) + \mathcal{O}\left(\frac{h^m}{\epsilon^m}\right).$$

For equidistant particle locations at spaces h in a d-dimensional space, the weights can be chosen as: $w_p = h^d f(\hat{\mathbf{x}}_p)$ with $m = \infty$ for certain kernels and for positive kernels such as the Gaussian, $r = 2$. Higher order representations can be constructed by allowing for negativity of the mollifier.[20,40]

These error estimates reveal an important, albeit often overlooked, fact for smooth particle approximations: to obtain accurate approximations, the distance between particles must be smaller than the size of the mollifier ($h/\epsilon < 1$), i.e. *smooth particles must overlap.*

2.1.1. *Particle derivative approximations*

Particle approximations of the derivative operators can be constructed through their integral approximations. For unbounded or periodic domains, this can be easily achieved by taking the derivatives of Eq. (2.1) as convolution and derivative operators

commute in this case. An alternative formulation involves the development of integral operators that are equivalent to differential operators such as the Laplacian for which Mas-Gallic introduced the method of Particle-Strength Exchange (PSE)[45]:

$$\Delta_\varepsilon f(\hat{\mathbf{x}}) = \varepsilon^{-2} \int (f(\mathbf{y}) - f(\hat{\mathbf{x}}))\eta_\varepsilon(\mathbf{y} - \hat{\mathbf{x}})\, d\mathbf{y},$$

where $\Delta_\varepsilon f(\hat{\mathbf{x}})$ denotes the mollified approximation of the Laplacian operator. High order approximations can be obtained by choosing suitable functions η_ϵ. The method can be extended to anisotropic diffusion operators (a very useful operator when considering diffusion on surfaces as we will see in later sections).[46] Starting from the PSE formulation, in Ref. 50 a general integral representation for derivatives of arbitrary order is presented. The error analyzis of particle derivative approximations strengthens the requirement for particle overlap. Analogous to the function approximation using particles, the integral 2.1.1 can be approximated with particle locations as quadrature points and particle strengths as quadrature weights:

$$(\Delta^{\varepsilon,h} q)(x_{p'}) = \varepsilon^{-2} \sum_p \left(Q_p - Q_{p'} \frac{v_p}{v_{p'}} \right) \eta^\varepsilon(x_{p'} - x_p), \tag{2.4}$$

where v_p is the volume associated with the particle p. We note here that the PSE particle approximation of diffusion is equivalent to various finite difference schemes for different kernels when the particles find themselves in distributed regularly on a grid. In particle methods the precise connectivity of the computational elements (as for example in finite difference methods) is not required in order to discretize the governing equations, but neighboring elements need to overlap in order to provide consistent approximations.

2.2. *Particle methods for advection-diffusion-reaction equations*

Advection-diffusion-reaction equations are one of the key models for pattern formation and morphogenesis. These equations can be expressed as

$$\frac{\partial \mathbf{Q}}{\partial t} + \operatorname{div}(\mathbf{UQ}) = \mathbf{F}(\mathbf{Q}, \nabla\mathbf{Q}, \ldots), \tag{2.5}$$

where $\mathbf{Q}$ is a scalar flow property (e.g. concentration) or a vector (e.g. momentum) advected by the velocity vector field $\mathbf{U}$. Equation (2.5) is an advection equation in conservation form and the right-hand side $\mathbf{F}$ can take various forms involving derivatives of $\mathbf{u}$ and depends on the physics of the flow systems that is being simulated. An example for $\mathbf{F}$ is the diffusion-reaction term as for example in Fisher's equation ($\mathbf{F} = \nabla^2\mathbf{Q} + \mathbf{Q}(1 - \mathbf{Q})$). The velocity vector field ($\mathbf{U}$) can itself be a function of $\mathbf{Q}$, which leads to *nonlinear* transport equations.

We first consider the case $\mathbf{F} \equiv 0$. The conservative form of the model can be translated in a Lagrangian framework by sampling the mass of $\mathbf{u}$ on individual points, or point particles whose locations can be defined with the help of Dirac δ-functions. Hence when $\mathbf{u}$ is initialized on a set of point particles it maintains this

March 15, 2011 6:53:58pm WSPC/103-M3AS 00543 ISSN: 0218-2025 1st Reading

description, with particle locations obtained by following the trajectories of the flow field:

$$\mathbf{Q}(\mathbf{x}, t) = \sum_p \alpha_p \delta(\mathbf{x} - \mathbf{x}_p(t)), \tag{2.6}$$

where

$$\frac{d\mathbf{x}_p}{dt} = \mathbf{U}(\mathbf{x}_p, t) \tag{2.7}$$

and α_p denote the particle weights. Typically, if particles are initialized on a regular lattice with grid size Δx, one will set $\mathbf{x}_p^0 = (p_1\Delta x, \ldots, p_n\Delta x)$ and $\alpha_p = (\Delta x)^d \mathbf{Q}(\mathbf{x}_p, t = 0)$. One may also write the weight of the particles as the product of the particle strength and particle volume that are updated separately: $\alpha_p = v_p\mathbf{u}_p$.

The set of equations can be solved by numerical quadrature, while recent efforts place particular emphasis on numerical integrators that preserve the geometric characteristics of this set of equations. Using smooth particles to solve (2.5) in the general case ($\mathbf{F} \neq 0$), one further needs to increment the particle strength by the amount that is dictated from the right-hand side $\mathbf{F}$. For that purpose, local values of $\mathbf{F}$ at particle locations multiplied by local volumes around particles are required. The local values of $\mathbf{F}$ can always be obtained from regularization formulas (2.1).

The volumes v of the particles are updated using the transport equation

$$\frac{\partial v}{\partial t} + \operatorname{div}\,(\mathbf{U}v) = -v \operatorname{div}\mathbf{U}. \tag{2.8}$$

The particle representation of the solution is therefore given by (2.6), (2.7) complemented by the differential equations

$$\begin{aligned} \frac{dv_p}{dt} &= -\operatorname{div}\mathbf{U}(\mathbf{x}_p, t)v_p = 0, \\ \frac{d\alpha_p}{dt} &= v_p\mathbf{F}_p. \end{aligned} \tag{2.9}$$

2.3. *The Lagrangian frame, particle distortion and remeshing*

Particle methods are well suited to the solution of the convection equation, as the nonlinear PDE is cast into a Lagrangian frame leading to a set of ODEs for the particle trajectories. It may seem that particle methods then have an advantage over their Eulerian counterparts, as they do not need to discretize the nonlinear advection term. This advantage is valid, albeit only when the velocity field is equivalent to a solid body translation or rotation. In more general cases, as particles follow the flow field, the locations of the particles can become distorted and the overlapping condition, necessary for the convergence of the particle approximation of the transported field, can be violated. The reconstruction (2.2) breaks down as ζ_ε is not well-sampled anymore and the method fails to converge.

There are several approaches that address this problem of Lagrangian distortion (see Ref. 41 and references therein). We advocate an approach that has been shown to be effective in simulating viscous vortical flows, that amounts to "remeshing" the particles by interpolating particle strengths onto a set of regular grid points that become subsequently the active particles:

$$\tilde{Q}_p = \sum_l Q_l M(\tilde{\mathbf{x}}_p - \mathbf{x}_l), \tag{2.10}$$

where the subscript l denotes the old particles that are remeshed and p the grid points that become the new particles. The interpolation kernel M is chosen, such that it conserves the discrete moments of Q_l:

$$\sum_p \tilde{Q}_p \tilde{\mathbf{x}}_p^{\alpha} = \sum_l Q_l \mathbf{x}_l^{\alpha}, \quad \text{for } 0 \le \alpha < \tilde{r}. \tag{2.11}$$

Note that the number of particle is not necessarily the same for the new and old set of particles. In multidimensions M is usually chosen as a tensor product of one-dimensional kernels. Replacing (2.10) into (2.11), for the 1D case, and $\tilde{x}_p = ih$ we obtain

$$\sum_i \sum_p Q_p M(ih - x_p)(ih)^{\alpha} = \sum_p Q_p x_p^{\alpha}. \tag{2.12}$$

For simplicity we consider $Q_p = \delta_{0p}$, so that (2.12) becomes

$$\sum_i M(ih - x_0)(ih)^{\alpha} = x_0^{\alpha}, \tag{2.13}$$

in other words: the requirement for polynomial reproduction.

The remeshing kernel should be chosen based on the nature of the problem that we want to solve. For example when we wish to have minimal numerical dissipation, it is crucial to employ a kernel which is interpolating while when considering problems that feature discontinuities a smoothing remeshing kernels should be used to avoid spurious oscillations. We present here a kernel that presents a compromise of the above two requirements, namely the M_6^* kernels that is nominally fourth-order accurate and has a support of 6:

$$M_6^*(x) = \begin{cases} -\dfrac{1}{12}(|x|-1)(25|x|^4 - 38|x|^3 - 3|x|^2 + 12|x| + 12) & |x| < 1, \\ \dfrac{1}{24}(|x|-1)(|x|-2)(25|x|^3 - 114|x|^2 + 153|x| - 48) & 1 \le |x| < 2, \\ -\dfrac{1}{24}(|x|-2)(|x|-3)^3(5|x|-8) & 2 \le |x| < 3, \\ 0 & 3 \le |x|. \end{cases} \tag{2.14}$$

March 15, 2011 6:54:00pm WSPC/103-M3AS 00543 ISSN: 0218-2025 1st Reading

This kernel was derived by requiring: $M_6^* \in C^2(\mathbb{R}^3)$, interpolation (or delta-Kronecker property), polynomial reproduction up to fourth order, even parity, and vanishing first and second derivatives at the end points ($x = \pm 3$).

3. Particles and Shapes

Particle methods offer a flexible way of discretizing and complex, deforming shapes (volumes and surfaces). Thinking particles, the first approach that comes to mind is to represent the surface of the geometry as a set of points in space. This surface can be deformed by simply moving these points with a given velocity. A simple query however, such as deciding whether we are within the geometry or outside calls for a notion of connectivity between the points, requiring that we perform a triangulation of this point set. When the geometry is subject to large deformations, one needs to resort to remeshing techniques, introducing new points in expansion zones, and removing points in compression zones.[92] When the geometries undergo topological changes, however, one needs to resort to heuristics. Methods that follow this line are called *interface tracking* or *front tracking* methods, they have been successfully applied to problems as diverse as multiphase flow,[155] drop breakup dynamics,[42] or solidification.[81] Particle methods can be combined with level sets in order to provide an implicit representation of surfaces and by distributing particles inside a surface we can discretize any function that is defined in the volume enclosed by the surface.

3.1. *Particles and level sets*

We begin by describing particle-level sets as introduced in Ref. 75. The level set method[110,143] is an interface capturing approach, where the geometry Γ is described implicitly as the zero isosurface of a level set function φ, i.e.

$$\Gamma = \{\mathbf{x} \,|\, \varphi(\mathbf{x}) = 0\}. \tag{3.1}$$

This level set function is chosen such that it represents a signed-distance function, defined by

$$|\nabla \varphi| = 1. \tag{3.2}$$

The interface Γ can be moved and deformed by making it subject to a simple advection equation, which is often called the "level set equation":

$$\frac{\partial \varphi}{\partial t} + \mathbf{u} \cdot \nabla \varphi = 0. \tag{3.3}$$

Surface properties can be retrieved directly from φ, e.g. the surface normal is given by $\mathbf{n} = \nabla \varphi|_\Gamma$, and the mean curvature by $\kappa = \nabla \cdot \mathbf{n}|_\Gamma = \Delta \varphi|_\Gamma$.

Level set methods have been successfully applied to a wide range of problems (see the textbook[111] and references therein). Most level set methods solve Eq. (3.3) in a Eulerian frame using finite-difference discretizations. A drawback of this approach is the inherent numerical diffusion associated with the discretization of

the convection term in Eq. (3.3). This numerical diffusion leads to the loss of small scale features in the geometry or interface that is represented by the level set. Several remedies have been proposed, most prominently the so-called "Particle Level Set Method" introduced by Enright *et al.*[53] This formulation employs a Eulerian representation of the level set function on a grid, and additionally uses marker particles, which are scattered around the interface and carry subgrid-scale information to maintain and reconstruct the interface. In Ref. 75 a truly Lagrangian particle level set method was introduced by Hieber and Koumoutsakos, which enjoys the characteristically small numerical diffusion errors of the Lagrangian particle approach.

Equation (3.3) can be discretized using a particle scheme:

$$\begin{aligned} \frac{d\varphi_p}{dt} &= 0, \\ \frac{d\mathbf{x}_p}{dt} &= \mathbf{u}(\mathbf{x}_p, t), \\ \frac{dv_p}{dt} &= (v_p \nabla \cdot \mathbf{u})(\mathbf{x}_p, t), \end{aligned} \tag{3.4}$$

and the function can always be reconstructed as

$$\varphi(\mathbf{x}, t) = \sum_p v_p \varphi_p M(\mathbf{x} - \mathbf{x}_p(t)), \tag{3.5}$$

where v_p denote the particle volumes. In principle, we would have to evolve the particle volumes as well in order to reconstruct φ, this however, is unnecessary if we perform renormalizations of the kernel M as described in Ref. 25, because the renormalization factor is equal to the particle volume: $\sum_p hM(x - x_p) = v(x)$.

The signed-distance property (3.2) of the level set has the following advantages: the distance to the interface can always be assessed in $\mathscr{O}(1)$ operations, which can be crucial for immersed interface applications (e.g. Sec. 4.2). The property (3.2) is also a condition on the regularity of the gradient, which can be crucial for stable computation of curvature and other higher-order surface properties.

The equation for the evolution of the signed-distance property, $\mathscr{M} \equiv \frac{1}{2}|\nabla\varphi|^2$ can be derived using (3.3) and results in

$$\frac{\partial \mathscr{M}}{\partial t} + \mathbf{u} \cdot \nabla \mathscr{M} = -2\mathscr{M}\mathbf{n} \cdot (\nabla \otimes \mathbf{u})\mathbf{n}, \tag{3.6}$$

so as soon as there is some deformation in the flow in normal direction, $\mathscr{M}$ derails exponentially from unity. Reinitialization is the periodically applied process of healing this divergence from the signed-distance property. There are many different approaches to this, they can however be classified into two broad categories: fast marching type methods (see Ref. 142 for a comprehensive review), and PDE-based methods.[149] Our experience with these techniques indicates that PDE based methods

March 15, 2011 6:54:02pm WSPC/103-M3AS 00543 ISSN: 0218-2025 1st Reading

provide more accurate reinitialization procedures over fast marching methods at the expense of computational cost.

In the context of morphogenesis, as described by reaction−diffusion equations on moving surfaces a novel scheme of reinitialization has been proposed in Ref. 25

$$\frac{\partial \varphi}{\partial \tau} + \varphi(1 - |\nabla \varphi|^{-1})|\nabla \varphi| = 0.$$

What is hidden in this Hamilton−Jacobi form is the following equivalent "advection" form:

$$\frac{\partial \varphi}{\partial \tau} + (\varphi - |\nabla \varphi|^{-1}\varphi)\mathbf{n} \cdot \nabla \varphi = 0.$$

There are no "reaction" terms in this formulation anymore, and the convection velocity is given as

$$\mathbf{u}_{\text{new}} = (\varphi - |\nabla \varphi|^{-1}\varphi)\mathbf{n}.$$

This formulation enables a higher accuracy of the WENO discretization and it may also serve as a good "preconditioner" for PDE based methods.

3.2. *Reaction diffusion systems on complex deforming geometries*

Bertalmio *et al.*[29] introduced a method to perform diffusion calculations on geometries that are represented by level sets in three dimensions. Xu and Zhao,[160] and Adalsteinsson and Sethian[5] later independently proposed a level set method for the transport of surface-bound substances on a deforming interface. Both works employed a non-conservative formulation based on level set interface capturing and showed results of passive advection of an interface with an associated surfactant.

We consider a reaction−diffusion system evolving on a smooth surface and for simplicity of presentation we will only consider homogeneous isotropic diffusion, with a coefficient D_s

$$\frac{\partial c_s}{\partial t} = F_s(\mathbf{c}) + D_s \Delta_\Gamma c_s, \tag{3.7}$$

where Δ_Γ denotes the Laplace−Beltrami operator on Γ. We are interested in solving this equation on surfaces that evolve with time, $\Gamma(t) = \{\mathbf{x}_\Gamma(t)\}$ with

$$\frac{d\mathbf{x}_\Gamma}{dt} = \mathbf{u}_n(\mathbf{x}, \mathbf{c}, \Gamma). \tag{3.8}$$

Following Ref. 146, using Eq. (3.8) we rewrite Eq. (3.7) as

$$\frac{\partial c_s}{\partial t} + ((\mathbb{1} - \mathbf{n} \otimes \mathbf{n})\nabla)(c\mathbf{u}) = F_s(\mathbf{c}) + D_s \nabla \cdot ((\mathbb{1} - \mathbf{n} \otimes \mathbf{n})\nabla c_s). \tag{3.9}$$

In order to solve this problem with particle methods we write Eq. (3.9) as a conservation law:

$$\frac{\partial c_s}{\partial t} + \nabla \cdot (c_s \mathbf{u}) = (\mathbf{u} \cdot \mathbf{n}) \frac{\partial c_s}{\partial n} + c_s \mathbf{n} \cdot (\mathbf{n} \cdot \nabla)\mathbf{u} + F_s(\mathbf{c}) + D_s \nabla \cdot ((\mathbb{1} - \mathbf{n} \otimes \mathbf{n}) \nabla c_s). \tag{3.10}$$

The reformulation from (3.9) to (3.10) necessitates the extension of both c_s and $\mathbf{u}$ from Γ to Ω. The primary requirement on this extension is that it be differentiable. However, inspecting the first two terms on the right-hand side of Eq. (3.10), we realize that if we extend c_s and $\mathbf{u}$ such that

$$\frac{\partial c_s}{\partial n} = 0 \quad \text{and} \quad \frac{\partial (\mathbf{n} \cdot \mathbf{u})}{\partial n} = 0, \tag{3.11}$$

we can simplify Eq. (3.10) to

$$\frac{\partial c_s}{\partial t} + \nabla \cdot (c_s \mathbf{u}) = F_s(\mathbf{c}) + D_s \nabla \cdot ((\mathbb{1} - \mathbf{n} \otimes \mathbf{n}) \nabla c_s). \tag{3.12}$$

Hence, ignoring the reaction terms, an extension satisfying (3.11), allows us to cast a conservation law on a deforming geometry as a conservation law in the embedding space Ω. This enables us to use known techniques to solve the equations in the (higher dimensional) embedding domain albeit at the expense of solving a nonlinear diffusion equation instead of the original linear equation.

Given that the surface itself is advanced by the level set Eq. (3.3), the particle discretization of Eq. (3.12) leads to the following system of ordinary differential equations:

$$\begin{aligned} \frac{d\mathbf{x}_p}{dt} &= \mathbf{u}(\mathbf{x}_p, t), \\ \frac{d\mathbf{C}_p}{dt} &= v_p \mathbf{F}(\mathbf{c}) + v_p \mathbf{D} \nabla^h \cdot ((\mathbb{1} - \mathbf{n} \otimes \mathbf{n}) \nabla^h \mathbf{c}), \\ \frac{dv_p}{dt} &= v_p \nabla \cdot \mathbf{u}. \end{aligned} \tag{3.13}$$

As we are solving the conservation law formulation (3.12), we need to extend both the concentrations $\mathbf{c}$ and the velocities $\mathbf{u}$ off the interface Γ, in a way that satisfies the requirements (3.11). As we are only interested in the concentrations on Γ, it suffices to extend the quantities into a narrow band around the level set (see Fig. 1), which we define as

$$\Gamma_e = \{\mathbf{x} \,|\, |\varphi(\mathbf{x})| \leq \gamma\}. \tag{3.14}$$

All calculations are restricted to this narrow band. The narrow-band thickness γ depends on the discretization of spatial operators, and is in general $\gamma < 10h$, where h is the spacing of the discretization. We periodically extend the concentrations by solving the following PDE[36,116]:

$$\frac{\partial c_s}{\partial \tau} + \operatorname{sign}(\varphi) \nabla \varphi \cdot \nabla c_s = 0, \tag{3.15}$$

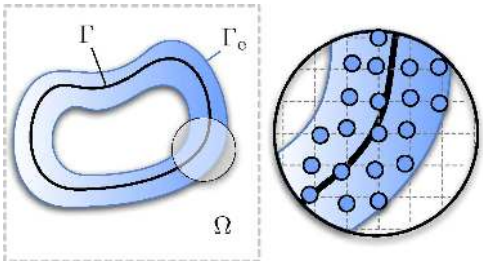

Fig. 1. Extension of the geometry Γ into Ω. Both the level-set function φ and the concentrations c_s are defined in the extended geometry Γ_e.

which leads to $\frac{\partial c_s}{\partial n} = 0$. We note that any other redistancing and extension scheme can be used instead, e.g. the Fast Marching Method.[142,111] In general, the same procedure also has to be applied to the velocity $\mathbf{u}$. In the case where the velocity only depends on $\mathbf{c}$, it suffices, however, to compute $\mathbf{u}$ from the extended $\mathbf{c}$.

4. Pattern Formation, Tumor Growth and Angiogenesis

We present here results from the application of the particle based framework to problems of reaction−diffusion on deforming surfaces, avascular tumor growth and angiogenesis.

4.1. *Reaction−diffusion systems on deforming geometries*

Initiated by the pioneering work of Turing,[154] a vast body of work has been devoted to the theoretical and computational aspects of pattern-formation in reaction−diffusion systems focusing mainly on local autocatalysis and long-range inhibition. The generation of stripe and spot patterns established by activator-inhibitor and activator-substrate systems was addressed in the review.[85] Reaction−diffusion systems on a sphere were investigated by Varea *et al.*[157] and Chaplain *et al.*[35] The former work considered a linearized Brusselator system whereas in Ref. 35 the Schnakenberg system was investigated in the context of tumor growth patterning through the distribution of growth factors along the tumor interface. Coupling of a pattern forming reaction diffusion systems to growth algorithms was presented in Refs. 71 and 77. The methods were used to simulate algal growth in two space dimensions and later coupled to a

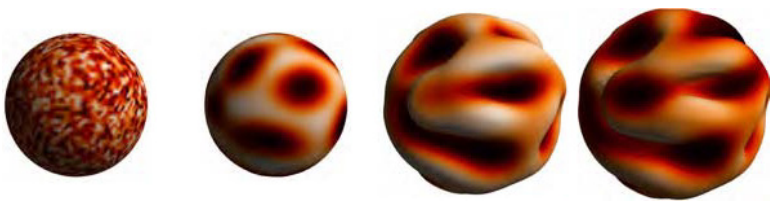

Fig. 2. Growth of the stripe pattern of system (4.1). Iterations 0, 50,000, 127,000 and 150,000.

Fig. 3. Spot pattern generated by solving Eq. (4.1) on a dumbbell shrinking under mean curvature flow.

triangulated representation of the geometry in order to extend to 3D.[72] In this system, however, only short simulations with small deformations were presented.

In the following, we consider a linearized version of the Brusselator[157] and the Koch−Meinhardt activator-substrate system[85] given by:

$$\begin{aligned} \frac{\partial c_1}{\partial t} &= \rho_1 \frac{c_1^2 c_2}{1+\kappa c_1^2} - \mu_1 c_1 + \sigma_1 + D_1 \Delta_\Gamma c_1, \\ \frac{\partial c_2}{\partial t} &= -\rho_2 \frac{c_1^2 c_2}{1+\kappa c_1^2} + \sigma_2 + D_2 \Delta_\Gamma c_2. \end{aligned} \tag{4.1}$$

The deformation of the evolving geometry is determined by the reaction−diffusion system via the local velocity $\mathbf{u}$ given as $\mathbf{u} = \mathbf{n} c_1$. An outward direction of the deformation is implied by $c_1 \geq 0$, that leads to an increase in surface area, in turn affecting the effective−diffusion constant in the reaction diffusion−system. We note that the only direct effect of growth on the reactions is a decrease of the concentration level that can be linked to a decay term that depends on the growth velocity. We present results that depict the evolution of these coupled simulations (2, 4) and illustrate the robustness of the method with respect to large changes in the geometry (3) (see also Ref. 27).

4.2. *Avascular tumor growth*

Mathematical modeling in the field of biology and medicine has traditionally been exploited to investigate the driving mechanisms in cancer growth. The ability to correctly model and predict the growth dynamics of cancer cell populations in silico could open new doors in understanding, diagnosing and treating the disease. While the biophysical processes that regulate and drive tumor progression are slowly being identified and understood, we start to model the problem of cancer growth by integrating a reduced set of identified key processes to gain insight on their explanatory power of the disease. Albeit the simplification of the underlying assumptions taken here, the presented framework may serve as a basis for model studies and extensions. We note here that the modeling work presented follows up on the work of Macklin and Lowengrub,[94] and Bearer *et al.*[21]

The model is based on a continuum formulation of a sharp interface separating cancerous from healthy tissue where the tumor tissue is modeled as an incompressible fluid. The tumor interface is implicitly modeled by a level set function, separating the computational domain into two distinct regions. Cell−cell adhesion is accounted

March 15, 2011 6:54:07pm WSPC/103-M3AS 00543 ISSN: 0218-2025 1st Reading

for by surface tension acting at the tumor boundary, mass sources and sinks are introduced inside the tumor interface to account for proliferation and cell death. Tumor cell faith is modeled to depend on the local nutrient level, inducing cell death (necrosis), rendering them quiescent or leading to cell growth (proliferation) depending on the local nutrient concentration. Nutrient concentration is assumed to be saturated inside the tissue surrounding the tumor and is transported into the tumor by means of diffusion where it is consumed by the tumor cells. In this work, we only consider one non-specific nutrient required by the tumor cells for viability and proliferation. Extensions of the work reported herein over the work presented in Ref. 94 lie in the extension of a 2D simulation to a 3D particle simulation and the adaption of the formulation that allows for the application of fast Poisson solvers that allow for large scale, parallel simulations. By introducing far-field boundary conditions, the presented implementation furthermore enables the investigation of effects of the tumor environment.

The reaction−diffusion system governing the evolution of the non-dimensionalized concentration c of nutrient satisfies:

$$\begin{aligned} \frac{\partial c}{\partial t} &= \nabla^2 c - c \quad \text{in } \Omega, \\ c|_\Gamma &= 1, \\ c &= 1 \qquad\quad \text{outside } \Omega, \end{aligned} \tag{4.2}$$

A necrotic core of dead cancer cell is formed in response to a drop of the nutrient concentration below the critical value N necessary for cell viability. The necrotic region is denoted by $\Omega_N = \{\mathbf{x}|c(\mathbf{x}) <\}$ separated from the viable tumor tissue by its boundary Γ_N. The solution of (4.2) does not depend on the position of the necrotic core and can be calculated solely on the position of the interface Γ of the living tumor cells. The healthy tissue surrounding the tumor is modeled as an infinite reservoir of nutrient by defining the boundary condition $c|_\Gamma = 1$.

Fig. 4. The Brusselator reaction−diffusion system was proposed in (Holloway *et al.*) as a patterning mechanism for plant growth. The system defines the dynamics of two species X and Y diffusing along a surface and reacting with each other and is known to produce stable patterns on a static surface. The snapshots show a realization of the model applied on a hemisphere. The color of the surface shows the species X (black is high, white is low) and the speed of deformation of the surface is proportional to X. While the surface deforms the reaction−diffusion system continuously changes the pattern which can lead to significantly different shapes.

Proliferation The tumor mass is modeled as an incompressible fluid retained by an implicit boundary exhibiting surface tension. In this model, we account for cell proliferation and cell death by adding and removing mass to the fluid, altering the non-dimensionalized pressure p inside the tumor. The solution of p depends on the solution of the nutrient concentration equation (4.2) and the tumor curvature κ at the interface Γ, satisfying

$$\begin{aligned} \nabla^2 p &= \begin{cases} -G(c-A) & \text{in } \Omega \text{ if } c \geq N, \\ GG_N & \text{in } \Omega \text{ if } c < N, \end{cases} \\ [p]|_\Gamma &= \gamma\kappa, \\ \nabla^2 p &= 0 \qquad\qquad \text{outside } \Omega, \end{aligned} \tag{4.3}$$

with the rate of apoptosis (cell death) A, the rate of proliferation (cell growth) G, the rate of volume loss due to necrosis (cell degradation) G_N and the nutrient threshold level N. The surface tension coefficient is further given by γ. The equation governing the outward normal velocity of the interface Γ is given by Darcy's law

$$U|_\Gamma = -\mathbf{n} \cdot \nabla p|_\Gamma = -\left.\frac{\partial p}{\partial n}\right|_\Gamma \tag{4.4}$$

with the pressure gradient ∇p at the interface location Γ. To initialize and track the interface Γ of the tumor, a level set function φ is introduced.

4.2.1. *Computational details*

We employ finite differences to solve for the reaction diffusion system (4.2), the reinitialization of the level set, the solution to the Poisson equation inside the computational domain $\mathscr{D}$ and the quantities $\mathbf{n} = \nabla\varphi$ and $\kappa = \nabla \cdot \mathbf{n}$ inside the narrowband around the interface Γ. In order to solve the pressure Eq. (4.3), we have to explicitly take into account the jump condition at Γ and provide appropriate boundary conditions. We enforce the jump condition at the tumor interface Γ by adding a correction term to all the grid points adjacent to the interface to account for the Laplace−Young jump condition given by

$$[p]_\Gamma = \gamma\kappa.$$

We enforce free space boundary conditions on $\mathscr{D}$ via the application of a far field Poisson solver[76,69] solving for the pressure without jump correction for particles located on the boundary of $\mathscr{D}$. We then take the solution at the domain boundary as Dirichlet boundary conditions for a finite differences based Poisson solver including the jump corrections and solve the system for all particles in $\mathscr{D}$.

We interpolate ∇p onto Γ, in order to evaluate Eq. (4.4) at the interpolation points and then extend it into a narrow band defined around Γ using the Hamilton−Jacobi-based extension method.[80,149] We apply a Gauss filter in order to attenuate the high-frequency errors in the pressure and curvature approximations.[94]

In a final integration step, particles that carry φ are created at grid locations inside the narrow band and then convected with U. The advanced level set location

March 15, 2011 6:54:08pm WSPC/103-M3AS 00543 ISSN: 0218-2025 1st Reading

of the next time step is recovered by remeshing the level set particles onto the computational grid. The signed distance property of the level set function inside the narrow band is reestablished via level set reinitialization.

4.2.2. *Avascular tumor growth with necrosis*

We illustrate results for a simulation of tumor growth with an amorphous initial condition subject to apoptosis in Fig. 5. The interface of the tumor is shown in beige whereas the red region inside the tumor marks the necrotic region at the core of the tumor. The parameters that determine the growth rate and necrosis in this simulation are set to $A = 0.5$, $G = 20$, $G_N = 1$ and $N = 0.5$. Although necrosis does slow down over-all tumor growth over time, it does not lead to complete growth inhibition.

The model presented here together with the methods implementing it can be seen as a first step towards macroscopic 3D tumor growth simulation. Furthermore, we found that albeit the implicit interface formulation using level sets, achieving level set joining is not inherent to the method proposed (see Ref. 25). A fact that has largely been neglected in simulations of tumor growth today is the appropriate modeling of

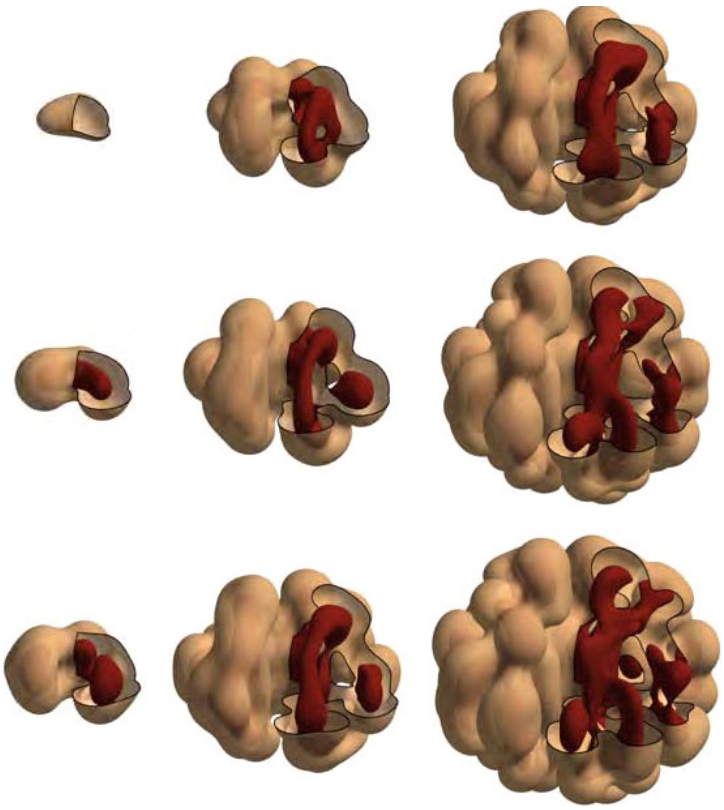

Fig. 5. (Color online) Tumor growth with amorphous initial condition and necrosis ($N = 0.5$). Pictures are taken at $t = 0, 1, 2, 3, 4, 5, 5.5, 6$ and 6.5.

March 15, 2011 6:54:09pm WSPC/103-M3AS 00543 ISSN: 0218-2025 1st Reading

the tumor microenvironment capturing the healthy tissue surrounding the tumor. We have addressed this issue in Ref. 25 (results not shown here) where we compare $p = 0$ boundary conditions on the tumor to the free-space formulation employed herein.

4.3. *Simulating sprouting angiogenesis*

Growth and formation of vascular networks in the human body can be observed under various conditions and is always linked to coordinated growth and migration of the endothelial cells constituting the blood vessel walls. The process where capillaries grow from a preexisting vasculature is referred to as sprouting angiogenesis, as opposed to the process of vasculogenesis, addressing the process of spontaneous network formation mainly observed during embryogenesis and intussusceptive angiogenesis, where existing vessels split in order to extend the vascular network structure. We note that sprouting angiogenesis can be observed in the human body under various conditions. In the work presented here, we focus on the process of tumor-induced angiogenesis initiated by a tumor in hypoxic conditions, secreting growth factors in order to establish means of nutrient and oxygen transport into the tumor.[57]

A tumor can assume a size of roughly $1\,\mathrm{mm}^3$,[56] satisfying nutrient support to the tumor cells by the sole means of diffusion from the surrounding tissue. Tumor progression at this stage leads to the formation of a necrotic region at the core of the tumor. As a result, apoptosis and necrosis inside and proliferation at the rim of the tumor are in balance, retaining the tumor from growing in size.[56] However, this condition of hypoxia can trigger the release of angiogenic growth factors such as Vascular Endothelial Growth Factors (VEGF) to name the most prominent amongst several.[55] Upon release, VEGF diffuses through the extracellular matrix (ECM) occupying the space in between the vasculature and the tumor, establishing a chemical gradient that triggers a directed angiogenic response at the nearby vasculature. Resulting in capillary growth towards the source of VEGF.

Receptor mediated VEGF signaling at the endothelial cells (ECs) triggers the release of proteases that degrade the basal lamina, the supporting scaffold around the vessel walls. This enables the ECs to leave their position in the vessel wall. In the following, coordinated proliferation and migration towards regions of higher VEGF concentration (chemotaxis) at the sprouting front leads to sprout extension of the vascular sprouts. The fibrous structure of the ECM composed of collagen fibers and matrix molecules such as Fibronectin has a guiding effect on the migrating endothelial cells, a contact and adhesion mediated cell guidance referred to as haptotaxis. Shortly after the initiation of this process, branching and loop formation, a process referred to as anastomosis, can be observed. In combination with lumen formation within the strands of endothelial cells, the established network allows for the circulation of blood. The process is completed by the rebuilding of a basal lamina and the recruitment of pericytes and smooth muscle cells stabilizing the vessel wall. However, in tumor induced angiogenesis, the vast amount of VEGF released by the tumor cells

March 15, 2011 6:54:10pm WSPC/103-M3AS 00543 ISSN: 0218-2025 1st Reading

leads to a disorganized and leaky vasculature resulting in inefficient blood supply. In combination with a growing tumor exerting pressure on the newly formed capillary network, even new regions of hypoxia arise, setting off the process of angiogenesis anew. Therefore, maturation is impaired leading to a sustained condition of angiogenesis.

As a consequence of the leaky vasculature the capillaries enable hematogenous spread of cancer cells that can lead to metastasis. Inhibition of angiogenesis restrains nutrient supply, and has been reported to reduce tumor growth and hinders migrating cells to metastasis in the tumor associated vasulature.[56] On the other hand, a complete inhibition promoting hypoxia could increase the occurrence of aggressive migrating tumor cell phenotypes.[14,117]

When addressing tumor-induced angiogenesis in a computational model, we refrain from including many biological processes involved, only addressing a limited number of processes dictated by the availability of biological data and the understanding of the key processes underlying the phenomena under investigation. Here we consider the migrative cell response as induced by the VEGF gradient, haptotaxis and the influence of the structural components of the ECM. VEGF is considered to appear in soluble and matrix bound isoforms. We explicitly consider the cleaving mechanism of matrix bound growth factors by EC released Matrix Metalloproteinases MMPs (see Fig. 6). For existing models of sprouting angiogenesis considering chemotaxis in response to soluble VEGF isoforms we refer to Refs. 17, 10, 34 and 148. Matrix bound isoforms of VEGF have been implicitly accounted for in the work by Bauer *et al.*[17] We note that the present model, to the best of our knowledge, is the first to include a cleaving mechanism in the presence of both VEGF isoforms. Haptotactic gradients are considered to be established by the release of Fibronectin.[10,34,148,17] In addition, we consider the binding of fibronectin to the ECM which localizes the haptotactic cues to the matrix fibers. We introduce an explicit model of the ECM

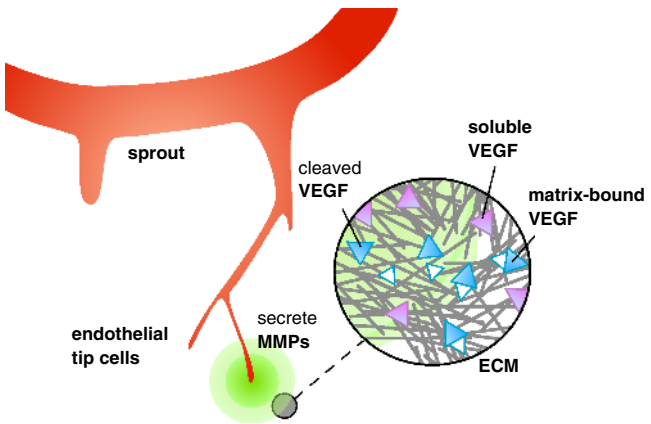

Fig. 6. Conceptual sketch of the different VEGF isoforms present in the ECM. Soluble and cleaved VEGF isoforms freely diffuse through the ECM, Matrix-bound VEGF isoforms stick to the fibrous structures composing the ECM and can be cleaved by MMPs secreted by the sprout tips.

consisting of fiber bundles modulating cell migration and growth factor distribution. Other modeling approaches explicitly considering the ECM have been proposed in Refs. 17 and 148.

We note that there exist a vast body of computational models in the field of sprouting angiogenesis. For an extensive overview of existing discrete, continuum and cell-based models of angiogenesis put in context to the work presented here, we refer to Ref. 101.

4.3.1. *A continuum modeling approach for mesenchymal cell motions*

We present model of sprouting angiogenesis based on a pure continuum description, which in contrast to prior models (with the exception of Ref. 17 does not rely on heuristic rules to obtain branching vessel morphologies. In this model, we hope to capture the core aspects governing mesenchymal motion including: (a) the structure of the extracellular matrix, (b) cell−matrix adhesion, (d) cell−cell adhesion, and (e) in addition to the effect of soluble growth factors the effect of matrix-bound growth factors on the chemotactic cell response using a subgrid-scale approach. We would like to motivate that the presented formalism can be applied to simulate mesenchymal cell migration in a more general context. Migration of invasive tumor cells into the healthy surrounding tissue and cell cluster migration as observed during gastrulation are just a few examples of where this model might be employed (see Fig. 7).

Representation of endothelial cells We choose to represent the endothelial cells by a density by function ρ. Evolution of the cell density in time is given by:

$$\frac{\partial \rho}{\partial t} + \nabla \cdot (\mathbf{a}\rho) = d\Delta\rho + R(\rho). \tag{4.5}$$

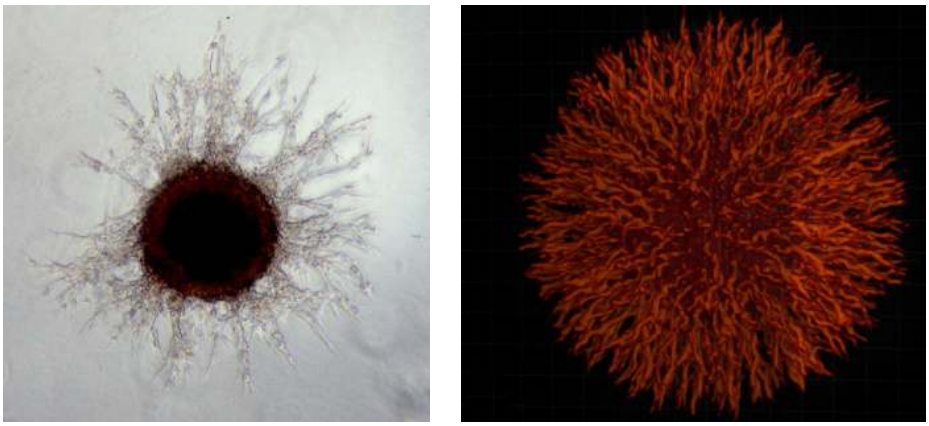

(a) (b)

Fig. 7. (a) A glioblastoma tumor spheroid, with invasive cells shed at its boundary (image from (TODO) [Habib:2003]). (b) Computer simulation of the shedding of invasive cells (see Sec. 4.3).

$\mathbf{a}$ denotes the cumulative effect of cell−cell adhesion $\mathbf{a}^{c/c}$, cell pressure $\mathbf{a}^{p}$ and $\mathbf{a}^{ecm,\phi}$ the migration cues induced by chemotaxis and the ECM. The right-hand side in (4.5) accounts for random cell migration and includes a reactive term to account for proliferation and cell death. In the presence of more than one cell concentrations, one density is used per cell line $(\rho_i)_{i=1}^{\#\text{CellTypes}}$. We note that in a continuum framework we could have chosen a level set approach to capture the interface of the cell density. However, when simulating highly elongated vessel like structures, the level set formulation is less favorable as it requires a narrow band of several grid spacing around each vessel, rendering the requirements for the resolution much higher than for the density based approach.

The Extracellular Matrix (ECM) The ECM occupies the space in between cells and is composed of fibrous structural components such as collagen, elastin and laminin.[44,84] The structural components serve as an adhesive scaffolding for migrating cells, enabling the cells to propel themselves along these structures. Most continuum models so far do not account for the guiding effects of matrix fibers on cell migration explicitly.

In this work, we propose to model the extracellular matrix as a collection of randomly distributed fiber bundles. The fiber bundles facilitate but also bias cell migration. The matrix is constructed by randomly distributing N_f fiber bundles of predefined length and width throughout the computational domain. We rasterize these bundles onto the ECM grid e and filter this field with a second-order B-spline kernel in order to attain a smooth, differentiable matrix representation.

Cell−cell adhesion Cell adhesion, a fundamental biophysical mechanism regulating tissue formation, stability, rearrangement and breakdown, is established by specific adhesion receptors of the cell. Integrin receptors located on the cell membrane may bind to fibronectin and collagen in the ECM, enhancing cell−matrix adhesion, whereas cell−cell adhesion is established via intercellular adhesion molecules such as cadherins. This transmembrane receptor mediated reaction is very local, as it happens upon contact. Our modeling approach is motivated by a set of requirements that aim to capture the main characteristics of cell adhesion: (a) cell adhesion happens locally over a short range. (b) adhesion induces movement of the cells towards the entity they adhere to. (c) cell movement in response to adhesion will decrease as the local cell density increases, ultimately coming to a complete stop when the local cell density reaches the close-packing density. Following these guidelines we model cell adhesion as an autocrine (in the case of one-cell population), or paracrine signaling f_i released by the cell population i

$$\begin{aligned} \mathbf{a}_i^{c/c} &= \sum_{j}^{\#\text{CellTypes}} \kappa_{ij} L(f_i, df_i) \nabla f_i, \\ \frac{\partial f_i}{\partial t} &= -\mu f_i + \alpha \left(1 - \frac{f_i}{f_{\max}}\right) \rho_i + D \Delta f_i, \end{aligned} \tag{4.6}$$

$L(f, df)$ is a cutoff function to keep the magnitude of the gradient bounded by df:

$$L(f, df) = df(\max(df, |\nabla f|))^{-1}. \tag{4.7}$$

Slow diffusion (D) in combination with a high decay coefficient (μ) keeps this artificial adhesion signal local. The release rate of f_i is given by α and k_{ij} describes the homotypic ($i = j$) and heterotypic ($i \neq j$) adhesion strength. So far, the model does not incorporate any repulsive effects a densely crowded cell population might excert. We incorporate these effects by adding a pressure-like term to the velocity:

$$\mathbf{a}^p = -\kappa_p H(\rho - \bar{\rho})\nabla\rho|\nabla\rho|^{-1}, \tag{4.8}$$

where $\rho \equiv \sum_i \rho_i$, κ_p is constant, $\bar{\rho}$ is the close-packing density and H the Heaviside function. We note that compared to existing continuum models of cell−cell adhesion,[12] the present model is less intuitive however more efficient and easier to implement.

The ECM, chemo- and haptotaxis We complete our model for mesenchymal cell migration by adding a formalism to account for chemotaxis, the main driving force in directed cell migration. The model for chemotaxis presented here is based on the most simple approach, where cells follow the gradient of a chemoattractant ϕ established via release at a tumor source subject to decay and diffusion. We bear in mind that this chemotactic response is but the most simple one, ignoring many effects such as membrane receptor saturation. This basic model of chemotaxis is extended to account for cell−matrix guidance, implementing the following assumptions: A cell will crawl along fibers that align with the guiding chemotactic gradient ($\nabla\phi$) leading to an increase in the cell migration speed. In addition, migrating cells rely on the presence of a fibrous scaffold to propel themselves. If there are no fibers ($e = 0$), a cell cannot migrate efficiently ($e_o \ll 1$). On the other hand, a very dense matrix ($e \approx e_\infty$) blocks cell migration and has to be degraded by the migrating cells, slowing down the effective migration speed. These assumptions are formulated as

$$\mathbf{a}_{\text{ecm},\phi} = \left[\left(1 - \left|\frac{\nabla e}{|\nabla e|} \cdot \frac{\nabla\phi}{|\nabla\phi|}\right|\right)\nabla e + \nabla\phi\right](e + e_o)(e_\infty - e), \tag{4.9}$$

and illustrated in Fig. 8.

Matrix-bound growth factors Vascular Endothelial Growth Factors exist in several different isoforms, some that are soluble and some that express binding domains to heparin binding sites inside the ECM.[120] These isoforms can bind to the matrix, retaining them form diffusing freely. Endothelial cells can release these matrix bound VEGF isoforms via the secretion of matrix metalloproteinases (MMPs) cleaving a shorter VEGF residue from the matrix bound molecule,[87] while conserving the cell signaling domain on the cleaved VEGF isoform. Once cleaved, the VEF becomes diffusible again and adds to the established VEGF gradient.

Although we do observe the formation of localized chemotactic cues around the pockets of matrix bound VEGF during simulation of the afore mentioned system

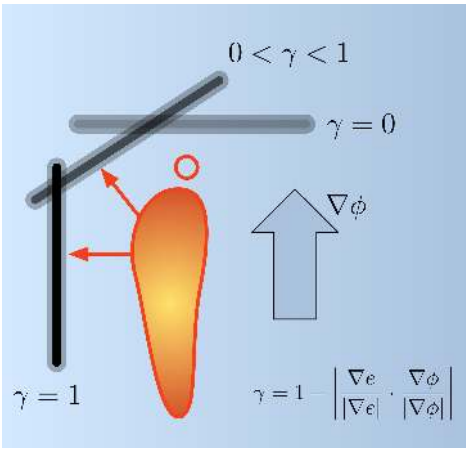

Fig. 8. A cell will move "onto" a fiber if the fiber direction is not transverse to the chemotactic gradient, i.e. the gradient of adhesion is not aligned with the chemotactic direction.

(see Fig. 9(a)), we do not observe an increase in the branching morphologies of the growing vasculature as suggested by *in vitro* and *in vivo* models of angiogenesis.[132,87] Taking a closer look at the matrix-bound VEGF distribution, we must realize that the modeled pocket size is too large to capture realistic distributions of bound VEGF in nature, where we expect the focus points of matrix-bound VEGF to be slightly

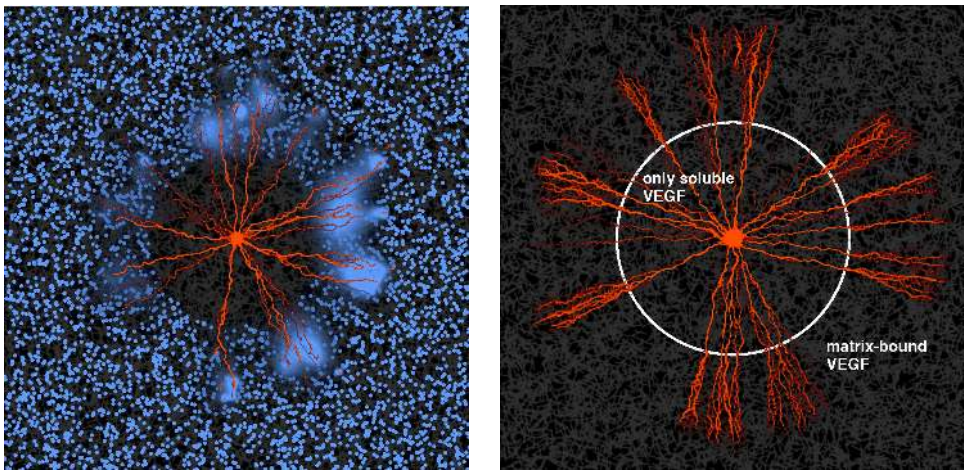

(a) (b)

Fig. 9. (a) Simulation with matrix-bound growth factors using pockets of matrix-bound VEGF distributed in the matrix. The endothelial cells release MMPs that cleave the bound growth-factors and make them soluble (diffuse blue cues) (b) Simulation with matrix-bound growth factors by the "diffusion" model. Within the white circle there are only soluble growth factors present, outside of the circle a constant concentration of growth factors is bound to the matrix. As apparent from the network structure, the matrix-bound growth factors lead to distinctively increased branching.

smaller than the cell scale. However, in a mesoscale continuum description, the incorporation of truly microscopic structures is not possible. For these reasons, we resort to a subgrid-scale modeling approach. We expect the cumulative effect of microscopic chemotactic queues on migrating cells to manifest itself at the mesoscopic level as an increase in random motion. We therefore model the presence of matrix-bound VEGF via the introduction of a spatially varying diffusion term d in Eq. (4.5). In the presence of only soluble VEGF isoforms, the diffusion term is zero. In the presence of matrix-bound VEGF isoforms, the diffusion term is increased locally depending on the matrix-bound VEGF concentration. This way, the release of MMPs along with the cleaving of matrix bound VEGF can be accounted for implicitly via a local modulation of the EC diffusion. We show that this system does lead to an increase in the observed branching frequency during simulation (see Fig. 9(b)). We like to point out that the branching behavior observed by this model is an output of the simulation, not relying on any formulation of heuristic branching rules.

4.3.2. *A hybrid model of sprouting angiogenesis*

To complement the purely continuum modeling approach presented in the previous section, we now present a deterministic, hybrid model of sprouting angiogenesis. The hybrid model description combines a continuum approximation of the molecular quantities such as VEGF, MMPs and fibronectin in addition to the endothelial stalk cell density with an agent-based particle representation for the actively migrating tip cells at the sprouting front. The particle based tip cell approach has been initially proposed in Ref. 119. The model has been introduced in Ref. 101 and we refer the reader to this original article for a more detailed description. As motivated in the previous section, also the hybrid model considers the presence of matrix bound VEGF isoforms and its cleaving by MMPs in the presence of an explicitly modeled ECM. Cell−cell adhesion and cell proliferation are accounted for implicitly via the migration speed of the tip cell particles and the underlying assumption that endothelial cells cannot break free from the existing vasculature. We introduce a set of rules that determine branching at the tip cells in response to divergence in the directional cues promoted by the VEGF and fibronectin gradients in combination with the ECM structure and considers the cell cycle to prevent branching events from happening right after branching has happened.[10,34,119] The model explicitly considers the extension of filopodia at the sprouting tips in order to probe the vicinity of the tip cells for migration cues. Although branching rules are formulated, the proposed model does not rely on branching probabilities.[10,34,119] In the following, we would like to direct the focus towards the modeling of the endothelial tip cell dynamics considered in cell migration, branching and anastomosis. For a detailed formulation of the reaction−diffusion system governing the VEGF, MMP and fibronectin evolution, we refer the reader to Ref. 101.

Extracellular Matrix Much like in the previous section, the ECM is modeled as a collection of fiber bundles randomly distributed throughout the computational

March 15, 2011 6:54:44pm WSPC/103-M3AS 00543 ISSN: 0218-2025 1st Reading

domain. In the context of the hybrid model, the ECM is given by a threefold representation: (a) a vector field $\mathbf{K}$ describing the fiber orientations, (b) an indicator function E_χ and (c) the fiber density filed E_ρ introduced in the previous section used to regulate the migration speed.

Tip Cell Migration Tip cell particle positions are given by $\mathbf{x}_p$. The tip cells migrate by updating the particle locations according to:

$$\frac{\partial \mathbf{x}_p}{\partial t} = \mathbf{u}_p, \quad \frac{\partial \mathbf{u}_p}{\partial t} = \mathbf{a}_p - \lambda \mathbf{u}_p, \tag{4.10}$$

with $\mathbf{u}_p$ and $\mathbf{a}_p$, the velocity and acceleration given at the particle location and the drag coefficient λ.

In this formulation, tip cell migration is guided by the gradients of VEGF and fibronectin gradients that establish the chemotactic and haptotactic migration cues.

$$\mathbf{a} = \alpha(E_\rho)\underline{\mathbf{T}}(\mathscr{W}([\text{VEGF}])\nabla[\text{VEGF}] + w_F \nabla[\text{bFIB}]). \tag{4.11}$$

We account for VEGF receptor saturation on the endothelial cells by introducing the response function

$$\mathscr{W}([\text{VEGF}]) = \frac{w_V}{1 + w_{V2}[\text{VEGF}]}, \tag{4.12}$$

with model parameters w_V and w_{V2}, attenuating the sensibility of the ECs to the VEFG gradient.

The presence of matrix fibers (E_ρ) is modeled to directly influence the cell migration speed, favoring a intermediate matrix density over a very dense or very sparse ECM.[59,44] This effect is captured in the function

$$\alpha(E_\rho) = (E_0 + E_\rho)(E_1 - E_\rho)C_1. \tag{4.13}$$

A threshold E_0 is introduced to define the migration factor in the absence of fibers. The maximal threshold density completely blocking migration is defined by E_1 where as C_1 denotes the ECM migration constant.

The directional cues that the fiber bundles exert on a migrating cells are captured by the tensor $\underline{\mathbf{T}}$ acting on the migration velocity

$$\{\underline{\mathbf{T}}\}_{ij} = (1 - \beta(E_\chi))\{\mathbb{1}\}_{ij} + \beta(E_\chi)K_i K_j, \tag{4.14}$$

with

$$\beta(E_\chi) = \beta_K E_\chi. \tag{4.15}$$

The ECM guidance strength is given by β_K and $\mathbf{K}$ denotes the vector field the tensor is applied on.

Branching and Anastomosis Migrating tip cells probe their environment for chemo- and haptotactic cues by extension of filopodia equipped with cell surface receptors.[61] Branching can be observed as a result of diverging migration cues detected by the

endothelial tip cells.[132] We introduce a curvature measure k in order to locate such regions of high anisotropy in the migration velocity field $\mathbf{V}$. In this model, we locate regions of high anisotropy in the migration acceleration direction field $\mathbf{V}$ by a curvature measure k.

$$k(\mathbf{x}) = \frac{\|\dot{L}(\mathbf{x}) \times \ddot{L}(\mathbf{x})\|}{\|\dot{L}\|^3}, \tag{4.16}$$

with $\mathbf{V} = (u, v, w)$, $\dot{L}(\mathbf{x}) = \mathbf{V}(\mathbf{x})$ and $\ddot{L} = u\mathbf{V}_x + v\mathbf{V}_y + w\mathbf{V}_z$.[158]

A branching event is triggered at tip cells where the local curvature k exceeds the predefined threshold level ai_{th}.

We introduce a model of filopodia extension in order to determine the preferred branching direction in 3D. To do so, for each tip cell sensing a high anisotropy k, six satellite particles are placed in a plane perpendicular to the current migration direction, radially distributed around the tip cell (Fig. 10). For each satellite particle, we measure the local velocity direction and calculate the angle between opposing satellite positions. The final branching direction is then determined by the satellite positions associated with the largest of these angles. In the following, a new tip cell is created and the tips are guided to sprout away from each other by modifying the velocity $\mathbf{u}_p$ on the right-hand side of (4.10) to $\mathbf{u}'_p$

$$\mathbf{u}'_p = \frac{|\mathbf{u}_p|}{1+\beta}\left(\frac{\mathbf{a}_s}{|\mathbf{a}_s|} + \beta\frac{\mathbf{x}_s - \mathbf{x}_p}{|\mathbf{x}_s - \mathbf{x}_p|}\right), \tag{4.17}$$

where $\mathbf{u}_s$ denotes the velocity at satellite position $\mathbf{x}_s$ and $\beta = 0.8$. This results in a short acceleration towards the satellite position. To account for the effect that ECs are insensitive to branching cues immediately after a branching event has occurred,[114]

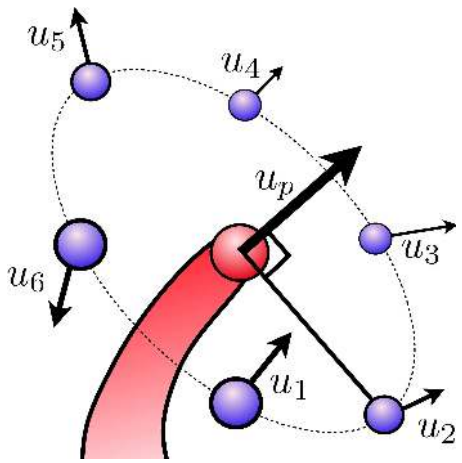

Fig. 10. The figure shows satellite particles placed in the plane perpendicular to the sprout migration direction. u_1 through u_6 describe the local migration cues at sprout particle location $\{B_1\}$.

March 15, 2011 6:54:58pm WSPC/103-M3AS 00543 ISSN: 0218-2025 1st Reading

a sprout threshold age sa_{th} is introduced. Sprouts do not branch again until they have reached the threshold age sa_{th}.

The formation of loops (anastomosis) occurs when tip cells fuse with either existing sprouts or with other tip cells.[114] In the event of a tip-sprout fusion, migration stops for the sprouting tip whereas after tip-tip fusion, one of the sprouts will continue to growth.

4.3.3. *Results*

In Ref. 101, we report results on the vessel morphology, branching frequencies and probabilities of anastomosis as influenced by large scale parametric studies of the structure of the ECM, the distribution of matrix-bound VEGF and the fibronectin mediated cell−cell and cell−matrix adhesion. The set of results along with the presented statistics provide a quantitative, comparative analyzis that may guide future experiments and simulations. The simulations successfully show that the extracellular matrix structure and density have a direct effect on endothelial cell migration and the number of observed branches corresponding to experimental observations made by Refs. 59, 44 and 141. In Fig. 11, we show the time course of one representative simulation of sprouting angiogenesis inside the explicitly modeled extracellular matrix. Furthermore, simulation results for tumor induced angiogenesis in the presence of matrix-bound growth factors show an increase in the number of observed branching structure and greatly influence vessel morphology. These results are in agreement with the findings made by Refs. 87 and 132 on vascular growth in the presence of matrix-bound VEGF. The fact that the statistical quantities we monitor do not depend on any probabilistic parameter may render the model easier to tune against experiments compared to most individual-based methods relying on such a parameter.

The novelty of this work lies in the consideration of both soluble and matrix bound growth factor isoforms and the explicit consideration of a fibrous ECM structure offering binding sites to molecular quantities such as fibronectin and VEGF while promoting guiding cues to the migrating cells. The grid free particle representation of the tip cells directly leads to the generation of smooth vessel networks. Grid based

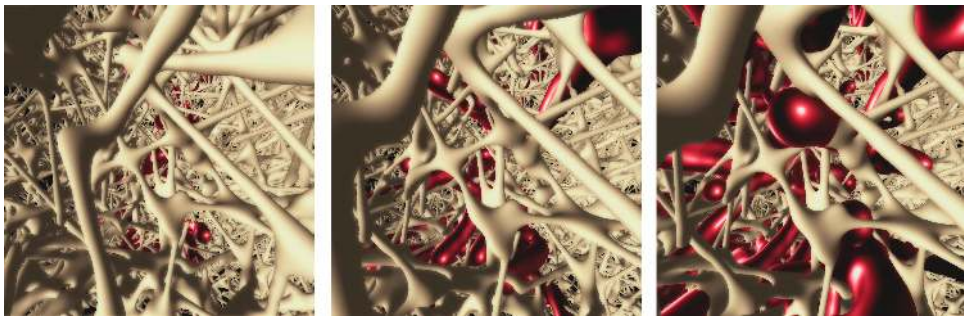

Fig. 11. Evolution of angiogenesis (red) along the fibers of the extracellular matrix (beige).

quantities and the particle based tip cell representation can be coupled via Particle to Mesh and Mesdh to Particle interpolation in a straightforward manner.

5. Stochastic Simulations

In this section, two algorithms for the simulation of reaction−diffusion processes — which were originally presented in Ref. 131 — are described, namely: (1) an accelerated spatially-dependent τ-leaping algorithm (called $S\tau$-leaping), and (2) a hybrid method (called $H\tau$-leaping) that combining a deterministic simulation of diffusion with a τ-leaping simulation of the chemical reactions. Fisher's equation is used to validate both algorithms. Furthermore, the role of the number of molecules in the system is explored in the pattern forming Gray−Scott equations.[115]

5.1. *Stochastic modeling of reaction−diffusion processes*

Reaction−diffusion phenomena in nature can be described by stochastic processes, where particles in a domain are subject to molecular collisions and movement via Brownian motion. In the present formulation, the domain is decomposed into equally-sized cells. Furthermore, it is assumed that a reactant molecule can react only with other reactants in its own cell, and diffusion events are modeled as unimolecular transitions to neighboring cells.

Consider a total of N species and a domain that has been discretized into a set of uniform cells denoted by $\mathbf{C}$, which subject to the same set of reactions, $\mathbf{R}$. Let $a_r(\mathbf{u}^c), r \in \mathbf{R}, c \in \mathbf{C}$, denote the propensity of the reaction r in the cell c and let $\nu_r^c = (\nu_{1r}, \ldots, \nu_{Nr})$ be the corresponding stoichiometric vector. The set of diffusion transitions is denoted by $\mathbf{D}$, and $\nu_d^{(i,c)}$ is the stoichiometric vector of the diffusion transition $d \in \mathbf{D}$ for the species i in the cell c. The reaction−diffusion process can be written in terms of of generic (chemical) transitions:

$$\sum_{i=1}^{N} \alpha_i^j A_i^j \to \sum_{i=1}^{N} \beta_i^j B_i^j, \quad j = 1, \ldots, M, \tag{5.1}$$

where j denotes the index of the transition, M is the number transitions, A_i is the species undergoing a transition, B_i is the species in the resulting transition, and α_i and β_i are the stoichiometric values. For example, the transitions for the pattern forming *Gray−Scott*[115] model can be expressed as:

$$U_0^{x,y,z} + 2\,U_1^{x,y,z} \to 3\,U_1^{x,y,z}, \tag{5.2}$$

$$U_1^{x,y,z} \to U_2^{x,y,z}. \tag{5.3}$$

Diffusion is recast as a set of transitions to neighboring cells, viz.:

$$U_i^{x,y,z} \xrightarrow{\frac{d_i}{dl^2}} U_i^{x-1,y,z}, \quad U_i^{x,y,z} \xrightarrow{\frac{d_i}{dl^2}} U_i^{x+1,y,z}, \tag{5.4}$$

$$U_i^{x,y,z} \xrightarrow{\frac{d_i}{dl^2}} U_i^{x,y-1,z}, \quad U_i^{x,y,z} \xrightarrow{\frac{d_i}{dl^2}} U_i^{x,y+1,z}, \tag{5.5}$$

$$U_i^{x,y,z} \xrightarrow{\frac{d_i}{dl^2}} U_i^{x,y,z-1}, \quad U_i^{x,y,z} \xrightarrow{\frac{d_i}{dl^2}} U_i^{x,y,z+1}, \tag{5.6}$$

where $U_i^{x,y,z}$ is the number of molecules of species i inside the cell indexed by (x, y, z), d_i is the macroscopic diffusion coefficient of species i, and dl is the cell size.

5.1.1. *Spatial τ-leaping*

Computationally efficient method for calculating the time-step for the τ-leaping method without the need for evaluating derivatives has been provided by Cao *et al.* in Ref. 32. Following Ref. 32, a bound is created for the molecular population in each cell:

$$\tau^{\text{reaction}} = \min_{c \in \mathbf{C}} \{\tau_c^{\text{reaction}}\}, \tag{5.7}$$

and for each cell we have

$$\tau_c^{\text{reaction}} = \min_{i \in \mathbf{I}} \left\{ \frac{\max\{\epsilon u_i^c / g_i, 1\}}{|\hat{\mu}_{i,c}^{\text{reaction}}(\mathbf{u})|}, \frac{\max\{\epsilon u_i^c / g_i, 1\}}{(\hat{\sigma}_{i,c}^{\text{reaction}}(\mathbf{u}))^2} \right\}, \tag{5.8}$$

where ϵ is an error control parameter where $0 < \epsilon \ll 1$, g_i is the *highest order of reaction*, $\mathbf{I}$ is the set of different species and $\hat{\mu}_{i,c}^{\text{reaction}}(\mathbf{u})$ and $(\hat{\sigma}_{i,c}^{\text{reaction}}(\mathbf{u}))^2$ are defined as:

$$\hat{\mu}_{i,c}^{\text{reaction}}(\mathbf{u}) = \sum_{r \in \mathbf{R}} \nu_{ir}^c a_r(\mathbf{u}^c), \tag{5.9}$$

$$(\hat{\sigma}_{i,c}^{\text{reaction}}(\mathbf{u}))^2 = \sum_{r \in \mathbf{R}} (\nu_{ir}^c)^2 a_r(\mathbf{u}^c). \tag{5.10}$$

The simple structure of the diffusion transitions can be used to accelerate the computation of $\tau^{\text{diffusion}}$

$$\tau^{\text{diffusion}} = \min_{c \in \mathbf{C}} \{\tau_c^{\text{diffusion}}\}, \tag{5.11}$$

$$\tau_c^{\text{diffusion}} = \min_{i \in \mathbf{I}} \left\{ \frac{\max\{\epsilon u_i^c, 1\}}{|\hat{\mu}_{i,c}^{\text{diffusion}}(\mathbf{u})|}, \frac{\max\{\epsilon u_i^c, 1\}}{(\hat{\sigma}_{i,c}^{\text{diffusion}}(\mathbf{u}))^2} \right\}. \tag{5.12}$$

The denominators can be computed as

$$\hat{\mu}_{i,c}^{\text{diffusion}}(\mathbf{u}) = \frac{1}{dl^2} \sum_{c' \in N(c)} u_i^{c'} - u_i^c, \tag{5.13}$$

$$(\hat{\sigma}_{i,c}^{\text{diffusion}}(\mathbf{u}))^2 = \frac{1}{dl^2} \sum_{c' \in N(c)} u_i^{c'} + u_i^c, \tag{5.14}$$

where $N(c)$ is the set of neighboring cells of c. As Eq. (5.14) will always be greater than Eq. (5.13), the formula for $\tau_c^{\text{diffusion}}$ can be simplified to:

$$\tau_c^{\text{diffusion}} = \min_{i \in \mathbf{I}} \left\{ \frac{\max\{\epsilon u_i^c, 1\}}{(\hat{\sigma}_{i,c}^{\text{diffusion}}(\mathbf{u}))^2} \right\}. \tag{5.15}$$

The time-step, τ, is chosen as the minimum of the two time-steps,

$$\tau = \min\{\tau^{\text{reaction}}, \tau^{\text{diffusion}}\}. \tag{5.16}$$

We perform the transitions on the entire solution, $\mathbf{u} = \{\mathbf{u}^c\}_{c\in\mathbf{C}}$, according to the following formula:

$$\mathbf{u}(t+\tau) = \mathbf{u}(t) + \sum_{c\in\mathbf{C}}\sum_{r\in\mathbf{R}} \nu_r^c \mathscr{P}(a_r(\mathbf{u}^c), \tau) + \sum_{c\in\mathbf{C}}\sum_{i\in I}\sum_{d\in\mathbf{D}} \nu_d^{(i,c)} \mathscr{P}\left(\frac{d_i u_i^c}{dl^2}, \tau\right), \tag{5.17}$$

where $\mathscr{P}(.)$ is a sample from a Poisson distribution.

5.1.2. *Hybrid τ-leaping*

In order to further accelerate the spatial modeling of reaction−diffusion systems, we proposed a hybrid scheme where the reactions are simulated stochastically while diffusion is simulated deterministically. This approximation is suitable since the diffusion process is typically two orders of magnitude faster than the reaction process.[28] We consider a system where the particles, $u_i = u_i(\mathbf{x}, t)$, evolve according to the following equation:

$$u_i(\mathbf{x}, t+\tau) = u_i(\mathbf{x}, t) + \mathscr{M}_1(d_i\Delta_d\mathscr{M}_2(u_i(\mathbf{x}, t))) + f_s^{(i)}(\mathbf{u}(\mathbf{x}, t)), \tag{5.18}$$

where $f_s^{(i)}$ represents the stochastically simulated reactions, Δ_d represents a deterministic diffusion operator, and $\mathscr{M}_1$ and $\mathscr{M}_2$ are mapping functions such that $\mathscr{M}_1$: $\mathbb{R}_+^N \to \mathbb{N}^N$ and $\mathscr{M}_2 : \mathbb{N}^N \to \mathbb{R}_+^N$.

$\mathscr{M}_1$ and $\mathscr{M}_2$ convert from between discrete and continuum representations of the field. $\mathscr{M}_2$ is trivial since in this mapping we have all the information that we need, i.e. converting from a discrete to a continuum model. This can be done by dividing the number of particles by the value P, the number of particles per unit of concentration. Care, however, needs to be taken with $\mathscr{M}_1$ since we need to ensure both a fair mapping and also a conservation of mass within our system.

The procedure for $\mathscr{M}_1$ is as follows: suppose we have a single species on a one-dimensional spatial domain where we denote x_i as the cell discretization of the domain, for $i = 1, \ldots, N$, $\Gamma(x_i) := \Delta_d\mathscr{M}_2(u(x_i, t))$, i.e. $\Gamma(x_i)$ is a concentration, and P the number of particles per unit of concentration. First, we lift the value of $\Gamma(x_i)$,

$$\hat{\Gamma}(x_i) = \Gamma(x_i)P. \tag{5.19}$$

$\hat{\Gamma}(x_i)$ can now be decomposed into a natural number part and a real part

$$\hat{\Gamma}(x_i) = \hat{\Gamma}_{\mathbb{N}}(x_i) + \hat{\Gamma}_{\mathbb{R}}(x_i), \tag{5.20}$$

where $\hat{\Gamma}_{\mathbb{N}}(x_i) \in \mathbb{N}$, $\hat{\Gamma}_{\mathbb{R}}(x_i) \in \mathbb{R}_+$, and more specifically $\hat{\Gamma}_{\mathbb{R}}(x_i) \in [0, 1)$. If we crop the values of $\hat{\Gamma}(x_i)$ such that

$$\hat{\Gamma}(x_i) = \hat{\Gamma}_{\mathbb{N}}(x_i), \tag{5.21}$$

then we can distribute the "extra molecules" L, where

$$L = \sum_{i=1}^{N} \hat{\Gamma}_{\mathbb{R}}(x_i), \tag{5.22}$$

where $L \in \mathbb{N}$. The objective now is to distribute these extra molecules by sampling from a probability density function where the probability of each cell is its fractional value $\hat{\Gamma}_{\mathbb{R}}(x_i)$. Therefore, we normalize all of the fractional values such that $p(x_i) = \frac{\hat{\Gamma}_{\mathbb{R}}(x_i)}{L}$. We denote the number of molecules gained for each cell i as k_i which is a realization of a random variable K_i, for $i = 1, \ldots, N$. We recall that a Binomial distribution, $\mathscr{B}(\mathscr{R}, \mathscr{P})$, is a discrete probability density distribution giving the number of successes in a sequence of $\mathscr{R}$ independent Bernoulli trials having a success probability of $\mathscr{P}$. We consider the fractional values as Bernoulli trials where the probability of success is $p(x_i)$, the probability of failure is $1 - p(x_i)$, and the number of trials is L. Therefore, the distribution of K_1 is $k_1 = \mathscr{B}(L, p(x_i))$, and all of the following variables $m \in \{2, \ldots, N\}$, denoted as K_m, are conditionally distributed on the previous events, i.e. on $\{k_1, \ldots, k_{m-1}\} = \{K_1, \ldots, K_{m-1}\}$. Therefore, for these variables we need to scale their probabilities of success based on the previous events, and decrease the amount of trials based on the previous events. Hence, we can sample from the following distribution:

$$k_m = \mathscr{B}\left(L - \sum_{j=1}^{m-1} k_j, \frac{p(x_m)}{1 - \sum_{j=1}^{m-1} p(x_j)}\right), \tag{5.23}$$

$$\hat{\Gamma}(x_i) = \hat{\Gamma}_{\mathbb{N}}(x_i) + k_i, \quad \text{for } i = 1, \ldots, N. \tag{5.24}$$

We note that at most $N - 1$ random numbers are needed and that the distribution of the molecules may terminate early if all L molecules have been distributed. It is also possible to distribute the L molecules in a pointwise manner instead of sampling from a Binomial distribution, but we have found that both L and the number of cells are large so that the method shown above is computationally more efficient.

The above equations trivially generalize to n dimensions where one has an n-dimensional space to distribute molecules instead of the one-dimensional example given above. For example, in three-dimensions where $x_{i,j,k}$ is the discretization of the domain, for $i = 1, \ldots, N_i$, $j = 1, \ldots, N_j$, and $k = 1, \ldots, N_k$, then Eq. (5.23) becomes

$$k_{a,b,c} = \mathscr{B}\left(L - \sum_{\alpha=1}^{a}\sum_{\beta=1}^{b}\sum_{\gamma=1}^{c-1} k_{\alpha,\beta,\gamma}, \frac{p(x_{a,b,c})}{1 - \sum_{\alpha=1}^{a}\sum_{\beta=1}^{b}\sum_{\gamma=1}^{c-1} p(x_{\alpha,\beta,\gamma})}\right), \tag{5.25}$$

and Eq. (5.24) becomes

$$\hat{\Gamma}(x_{i,j,k}) = \hat{\Gamma}_{\mathbb{N}}(x_{i,j,k}) + k_{i,j,k}, \quad \text{for } i = 1, \ldots, N_i, \quad j = 1, \ldots, N_j, \quad \text{and} \quad k = 1, \ldots, N_k. \tag{5.26}$$

The function $\mathbf{f}_s$ performs an independent τ-leaping procedure at the points $\mathbf{x}$ at time t with a time step of τ. Prescribing τ is performed by binding the changes in molecular populations, as described in the previous section, at each cell. The final τ is chosen as the minimum of all of these independent evaluations, and this τ is used as the time step for all of the τ-leaping procedures at each discretized volume.

The algorithm for the hybrid method is straightforward at this point. We choose a value for τ and simulate the reactions in our volume. Then, using this τ, we may simulate the diffusion process. This procedure is performed iteratively until the final integration time is reached.

Note that the speed-up of this hybrid approximation lies not only in that deterministic diffusion is more efficient than sampling random numbers (either by a random walk or τ-leaping), but also because we only need to diffuse such that our numerical stability criterion for our deterministic diffusion scheme is satisfied. In other words, we do not necessarily need to diffuse after every reaction process.

Pattern-formation equations have been proposed as models for morphogenesis.[154] It has been postulated that these simple reaction−diffusion systems are sufficient for describing the imperative characteristics of biological processes. Depending on how the parameters are chosen, and the size of the domain, one can obtain a multitude of patterns that may mimic natural phenomena. The *Gray−Scott* model is an example of self-organization in non-equilibrium, chemically reacting systems.[115] The partial differential equations for this model are

$$\frac{\partial u^{(1)}}{\partial t} - D^{(1)}\Delta u^{(1)} = -\rho\, u^{(1)} u^{(2)\,2} + F(1 - u^{(1)}), \tag{5.27}$$

$$\frac{\partial u^{(2)}}{\partial t} - D^{(2)}\Delta u^{(2)} = \rho\, u^{(1)} u^{(2)\,2} - (F + \kappa) u^{(2)}, \tag{5.28}$$

where $u^{(s)}$ denotes the sth species, and $D^{(s)}$ the diffusion coefficient for the sth species. The following chemical reactions represent the discrete model:

$$U_{\mathbf{i}}^{(1)} + 2\,U_{\mathbf{i}}^{(2)} \xrightarrow{\rho} 3\,U_{\mathbf{i}}^{(2)}, \tag{5.29}$$

$$\emptyset \xrightarrow{F} U_{\mathbf{i}}^{(1)}, \tag{5.30}$$

$$U_{\mathbf{i}}^{(1)} \xrightarrow{F} \emptyset, \tag{5.31}$$

$$U_{\mathbf{i}}^{(2)} \xrightarrow{F+\kappa} \emptyset, \tag{5.32}$$

where $U_{\mathbf{i}}^{(s)}$ is the number of molecules of species s in volume element $\mathbf{i} = (i_x, i_y, i_z)$. The values of F, ρ, κ, the diffusion coefficients, as well as the size of the domain determine what kind of pattern will appear.

Numerical simulations of the Gray−Scott equations in two and three-dimensions were performed with periodic boundary conditions using deterministic, $H\tau$-leaping (Sec. 5.1.2), and $S\tau$-leaping approaches (Sec. 5.1.1) with varying levels of particles

March 15, 2011 6:55:10pm WSPC/103-M3AS 00543 ISSN: 0218-2025 1st Reading

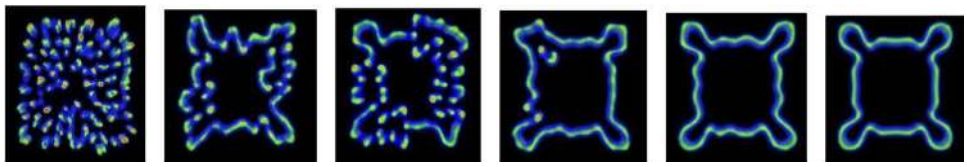

Fig. 12. Analyzis of the role of the number of particles for the Gray−Scott equations solved with a 300×300 discretization with $F = 0.04, \kappa = 0.06, t = 1000$. From left to right the number of particles per unit of concentration is increased from $100, 1000, 1000, 5000, 10000$, continuum, respectively. The methods used to solve the equations were the following (from left to right): $S\tau$-leaping, $S\tau$-leaping, $H\tau$-leaping, $S\tau$-leaping, $H\tau$-leaping, deterministic.

in order to determine whether one can obtain qualitatively different patterns. Two-dimensional simulations of the Gray−Scott equations are shown in Fig. 12. The number of particles in each cell were varied whilst keeping $F = 0.04, \kappa = 0.06$ and $\rho = 1$. Integration was performed from $t = 0$ to $t = 1000$. Notable differences in the solutions can be observed, namely the stochastic simulations converge to the pattern observed by purely deterministic simulations of reactions and diffusion as the number of particles increases.

The Gray−Scott equations in three-dimensions were also simulated using a discretization of $128 \times 128 \times 128$ with $F = 0.04, \kappa = 0.06$ and $\rho = 1$, and integrated from $t = 0$ to $t = 1000$ (Fig. 13). In three-dimensions, the noise from the low numbers of particles makes itself evident and the solution notably differs from the deterministic solution.

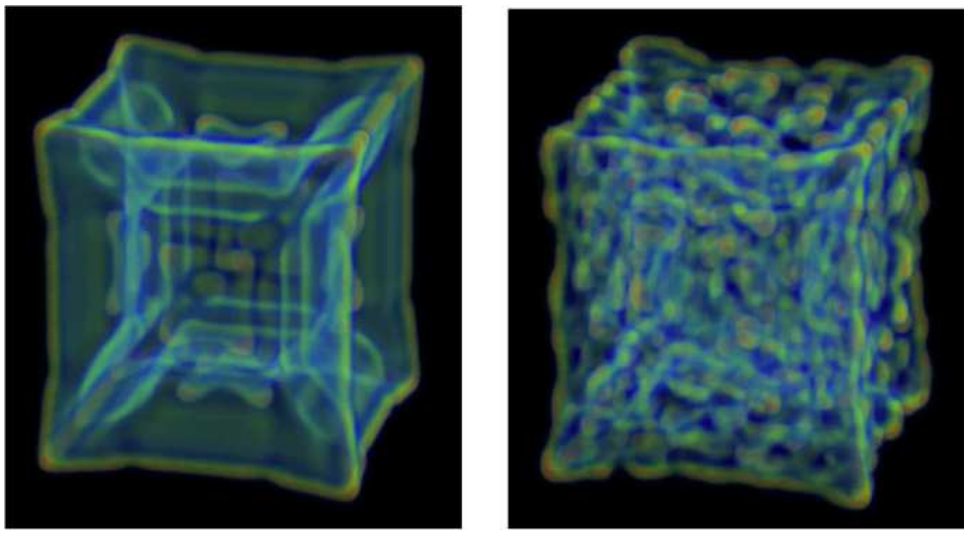

Fig. 13. Three-dimensional solutions of the Gray−Scott equations using (left) deterministic solver and $H\tau$-leaping solver (right) on a $128 \times 128 \times 128$ discretization with $F = 0.04, \kappa = 0.06, \rho = 1, t = 1000$. The $H\tau$-leaping method was performed with 1000 particles per unit of concentration.

5.2. *Stochastic simulations of glioblastomas*

The type of tumor considered here is the glioblastoma (glioma), which is the most malignant and most common brain tumor. The tumor is known to disseminate quickly throughout the brain and for this reason they are tumors with, as J. D. Murray states,[105] "a depressingly dismal prognosis for recovery". Indeed, if a glioma is left untreated, the median survival time is roughly 6 to 12 months.[105] Surgical removal of the tumor is presently the most effective treatment, thereby increasing the median survival time by 2.5 months.[3]

The human brain consists of grey and white matter, the former of which is composed of neuronal and glial cell bodies that are responsible for controlling brain activity, while the latter is composed of fiber tracts of neuronal axon bundles. Since white and grey matter are fundamentally different, it is not surprising that the rate of dissemination is different in the white matter than in the grey matter.[105]

In order to model the dissemination and proliferation of tumor cells in the brain, we begin by modeling the dissemination of cells with a diffusive term and will deal with the proliferation of cells later. The diffusion process is modeled by the following partial differential equation:

$$\frac{\partial u}{\partial t} = \frac{\partial}{\partial x}\left(D(x)\frac{\partial u}{\partial x}\right), \quad x \in \mathscr{D}, \tag{5.33}$$

$$\frac{\partial u}{\partial x} = 0, \quad x \text{ on } \partial\mathscr{D}, \tag{5.34}$$

where $\mathscr{D} = [0, 1]$. At the moment we shall confine ourselves to the 1D situation. The diffusion coefficient depends on x since it has been shown that proliferation is faster in the white matter than the grey matter, viz:

$$D(x) = \begin{cases} D_{\mathrm{g}} & \text{if } x \in \mathscr{D}_{\mathrm{grey}}, \\ D_{\mathrm{w}} & \text{if } x \in \mathscr{D}_{\mathrm{white}}, \end{cases} \tag{5.35}$$

where $\mathscr{D} = \mathscr{D}_{\mathrm{grey}} \cup \mathscr{D}_{\mathrm{white}}$, and where D_{g} and D_{w} are constants.

5.2.1. *Inhomogeneous diffusion*

Let $u_i(t) \triangleq u(x_i, t)$ where i is the index of a node. Using an explicit Euler method for the time-integration, the numerical method becomes

$$u_i(t + \Delta t) = \frac{\Delta t}{h^2} \sum_{\{j\,:\,j \in N(i)\}} D_{i,j}(u_j(t) - u_i(t)), \tag{5.36}$$

where $N(i)$ denotes the set of indices that are neighbors of cell i. The diffusion coefficient across the interface of cells i and j, denoted by $D_{i,j}$, needs to be defined. Following Ref. 102, a harmonic mean can be used, namely

$$D_{i,j} = \frac{1}{|x_i - x_j|} \int_{x_i}^{x_j} \frac{1}{D(s)} \mathrm{d}s, \tag{5.37}$$

which, if the mesh is uniform, can be integrated analytically and becomes:

$$D_{i,j}^{(\text{harmonic})} = 2\left(\frac{1}{D_i} + \frac{1}{D_j}\right)^{-1}. \tag{5.38}$$

5.2.2. *Boundary conditions*

To handle the Neumann boundary conditions, we use a ghost-point method. Consider the stencil at the left boundary:

$$u_0(t+\Delta t) = \frac{\Delta t}{h^2}(D_{0,1}u_1(t) - 2D_{0,0}u_0(t) + D_{0,-1}u_{-1}(t)) + \mathscr{O}(h^2), \tag{5.39}$$

where there is a ghost point at $x_{-1} = -h$. The derivative across the boundary needs to be zero, in which case we may use a central finite difference scheme for the gradient across the boundary:

$$\frac{u_1(t) - u_{-1}(t)}{2h} + \mathscr{O}(h^2) = 0, \tag{5.40}$$

or simply $u_1(t) = u_{-1}(t)$. Substituting this into the stencil yields the scheme at the boundary:

$$u_0(t+\Delta t) = \frac{2\Delta t}{h^2}(D_{0,1}u_1(t) - D_{0,0}u_0(t)) + \mathscr{O}(h^2). \tag{5.41}$$

5.2.3. *3D simulations using MRAG*

We consider the same inhomogeneous Fisher–Kolmogorov reaction–diffusion equation that Swanson *et al.* considered in Ref. 150:

$$\frac{\partial u}{\partial t} = \nabla \cdot (D(\mathbf{x})\nabla u) + \rho u(1-u), \tag{5.42}$$

where $u = u(\mathbf{x}, t)$, $\mathbf{x} \in \mathscr{D}$, the term $\rho u(1-u)$ represents the proliferation of cells, and

$$D(\mathbf{x}) = \begin{cases} D_{\text{g}} & \text{if } \mathbf{x} \in \mathscr{D}_{\text{grey}}, \\ D_{\text{w}} & \text{if } \mathbf{x} \in \mathscr{D}_{\text{white}}, \\ 0 & \text{if } \mathbf{x} \notin \mathscr{D}_{\text{grey}} \cup \mathscr{D}_{\text{white}}. \end{cases} \tag{5.43}$$

Equation (5.42) will be solved inside a realistic model of the human brain. The anatomy of the human brain comes from the biological database *Brain Web*.[1] The Brain Web database was created using a *Magnetic Resonance Imaging* (MRI) simulator and defines the distributions and locations of various elements of the brain on a 3D grid. At each voxel a concentration of grey and white matter is provided (along with fat, muscle/skin, skull, etc.), which will be used to define the geometry of a human brain.

The value of the diffusion coefficients at each voxel are

$$D_i \triangleq p_i^{(\text{w})} D_i^{(\text{w})} + p_i^{(\text{g})} D_i^{(\text{g})}, \tag{5.44}$$

where $p_i^{(w)}$ and $p_i^{(g)}$ are the relative fractions of white and grey matter, respectively, from the Brain Web database such that inside of the brain $p_i^{(w)} + p_i^{(g)} = 1$. The values of $D_i^{(g)} = 1.3 \cdot 10^{-3}\,\mathrm{cm}^2/\mathrm{day}$, $D_i^{(w)} = 5D_i^{(g)}$, and $\rho = 1.2 \cdot 10^{-2}/\mathrm{day}$ were taken from Ref. 105. These rates are used to model highly invasive tumor cells.

In order to define a stochastic process, we must define the drift process and multiplicative factor for the fluctuations. Moreover, we will use a multiresolution wavelet based framework (MultiResolution Adaptive Grids, *MRAG*,[130]) to solve the 3D equations that we will formulate in this section. The MRAG framework operates on blocks of meshes that locally have uniform resolutions and exploits parallel computing architectures. The equations must therefore be formulated independent of neighboring cells. With this in mind, we will formulate a non-conservative and local stochastic differential equation to model the dissemination and proliferation of a highly invasive brain tumor.

The drift of the stochastic process, μ, is defined as

$$\mu(u_i) = \begin{cases} h^{-2} \displaystyle\sum_{\{j\,:\,j \in N(i)\}} D_{i,j}^{(\mathrm{harmonic})}(u_j - u_i) + \rho u_i(1 - u_i), \\ \Delta_+ + \Delta_- + \rho u_i(1 - u_i), \end{cases} \tag{5.45}$$

where the Laplace operator has been split into positive Δ_+ and negative components Δ_-, i.e. the incoming and outgoing fluxes. Equation (5.45) can be written as

$$\mathrm{d}u_i = \mu(u_i)\mathrm{d}t. \tag{5.46}$$

A Brownian motion term is added to construct a stochastic differential equation

$$\mathrm{d}u_i = \mu(u_i)\mathrm{d}t + \sigma(u_i)\mathrm{d}B_t, \tag{5.47}$$

where we must now define the multiplicative factor $\sigma(u_i)$ for the fluctuations. The diffusion process is modeled as transitions to neighboring cells, where the fluctuations are transitions from or into a cell. Here we formulate the fluctuations as being proportional to the incoming transitions, namely $\sigma_1(u_i(t)) = \sqrt{\Omega\Delta_+}$. The numerical method is

$$\begin{aligned} u_i(t + \Delta t) = u_i(t) &+ \Delta t\ \mu(u_i(t)) \\ &+ F[\Omega^{-1}\sqrt{\Delta t}\sigma_1(u_i(t))\xi + \Omega^{-1}\sqrt{\Delta t}\sigma_2(u_i(t))\eta], \end{aligned} \tag{5.48}$$

where ξ and ν are random variates from a standard normal distribution and $\sigma_2(u_i(t)) = \sqrt{\Omega u_i(t)(1 - u_i(t))}$. Because of the instability of Fisher's equation, we have used $F[\cdot]$ which is a rounding operator that rounds to the nearest n/Ω, where $n \in \mathbb{Z}$, i.e. the fluctuations are on the order of particles in the system so as to not spuriously heat up the leading edge of the front. In principle, Ω should be the number of tumor cells, where the number of tumor cells in a real tumor is 10^{11}.[105] The value of Ω was set to 10^7 per unit of concentration per node which is, however, lower than a total of 10^{11}. We note that the fluctuations are on the order of 10^{-3} or 10^{-4} (i.e. $\Omega^{-1/2}$). A simulation over a time period of two years is shown in Fig. 14. The initial condition was a point source at an arbitrary position in the brain.

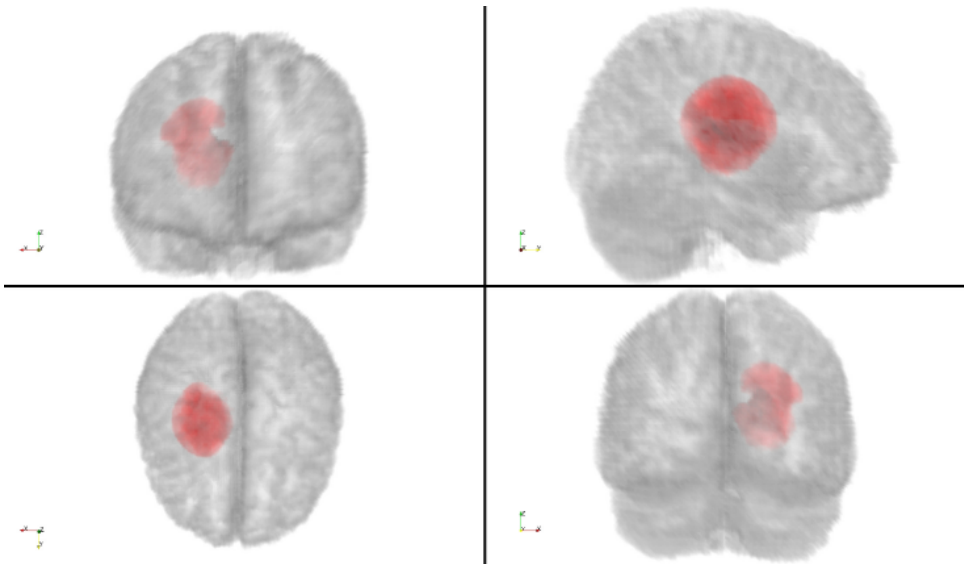

Fig. 14. (Color online) Virtual glioma at time $t = 720$ days: tumor density (red), gray matter, and white matter.

It can be seen that the growth pattern of the tumor is nontrivial and is highly dependent on the anatomy of the brain and initial position of the tumor. Specifically, the location of the white and grey matter tissues dictates the growth process. The results presented here used the same model as the one considered in Ref. 150, however, here a different numerical method as used. Here the harmonic average is used for the discontinuous diffusion coefficient and a stochastic numerical integration scheme as used. Moreover, both models make significant assumptions about the growth of tumors. The fundamental assumptions are (1) exponential or logistic proliferation of tumor cells for growth and (2) diffusion as an approximation for cell motility.

6. Particle Models for Discrete Systems

Many particle systems (Potts Models, Dissipative Particle Dynamics, Stochastic Simulation Algorithms) model complex system behavior through the formulation of deterministic or stochastic discrete rules between interacting particles. The particles are characterized by their geometrical shape and transported quantities such as density, chemical composition etc. These systems represent a synthetic computational approach identifying biological cells with individual particles and they can accommodate cell properties of adhesion, growth rate and elasticity. Many particle systems are well suited to simulations in complex deforming domains and they can be extended to incorporate reaction−diffusion processes involved in gradient formation as well as signaling pathways. We note that recently a vertex model, accommodating cells of different shapes, was implemented in order to study the physical basis of epithelial cell packing in the third instar larval wing disk of Drosophila.[6]

March 15, 2011 6:55:30pm WSPC/103-M3AS 00543 ISSN: 0218-2025 1st Reading

Particle models amount to tracking the locations $\mathbf{r}_i$, $i = 1, \ldots, N$, of N particles by solving numerically Newton's equations of motion:

$$m_i \frac{d^2 r_i}{dt^2} = \mathbf{F}(r_i, r_j, m_i, m_j, \ldots), \tag{6.1}$$

where $\mathbf{F}$ denotes the force field that can be derived as the gradient of a potential energy U. It is important to note here that the approximate integration of these equations makes the trajectories sensitive to perturbations in the initial conditions. Particle trajectories should not be viewed as exact representations of the trajectories of the systems they aim to model, but rather as their statistical representations. The more reliable diagnostics that can be gleaned from these trajectories are those obtained by suitable spatial and temporal averages. The potential energy function (U) whose gradient provides us with the force field ($\mathbf{F}$) give a description of the relative energy or forces of the ensemble for any geometric arrangement of its constituent particles. This description may include energy for bending, stretching and vibrations of the particles, and interaction energies between the molecules. Classical force fields are usually built up as composite potentials, i.e. as sums over many rather simple potential energy expressions. Mostly pair potentials $V(r_{ij})$ are used, but in the case of systems where bonds are determining the structure, multi-body contributions $V(r_{ij}, r_{ik})$, and $V(r_{ij}, r_{ik}, r_{il})$ may also enter the expression, thus

$$U = \sum_{i,j} V(r_{ij}) + \sum_{i,j,k} V(r_{ij}, r_{ik}) + \sum_{i,j,k,l} V(r_{ij}, r_{ik}, r_{i,l}), \tag{6.2}$$

where $r_{ij} = |\mathbf{r}_i - \mathbf{r}_j|$ is the distance between ith and jth atoms. The contribution to the interaction potential can be ordered in two classes: intramolecular and intermolecular contributions. While the former describe interactions which arise in bonded systems, the latter are usually pair terms between distant atoms. Various intramolecular potentials are used to described the dynamics of chemical bonds and their interactions. The potential

$$V(r_{ij}) = \frac{1}{2} K_h (r_{ij} - r_0)^2, \tag{6.3}$$

is developed from a consideration of simple harmonic oscillators,[54] where r_{ij} and r_0 denote the bond length and the equilibrium bond distance, respectively. The force constant of the bond is given by K_h. Alternatively, the Morse potential[104]

$$V(r_{ij}) = K_M (e^{-\beta(r_{ij} - r_0)} - 1)^2, \tag{6.4}$$

is used, allowing for bond breaking. Here K_M and β are the strength and distance related parameters of the potential.

For coordination centers, i.e. atoms where several bonds come together, usually bond angle terms are applied including harmonic bending via

$$V(\theta_{ijk}) = \frac{1}{2} K_\theta (\theta_{ijk} - \theta_c)^2, \tag{6.5}$$

or the harmonic cosine bending via

$$V(\theta_{ijk}) = \frac{1}{2} K_\theta (\cos\theta_{ijk} - \cos\theta_c)^2, \tag{6.6}$$

where θ_{ijk} is the angle formed by the bonds extending between the ith, jth, and kth atoms, and θ_c is the equilibrium angle. Dihedral bond potentials are often employed for systems involving chains of bonded atoms, to ensure a consistent representation over several centers[97,134]

$$V(\phi_{ijkl}) = \frac{1}{2} \sum_{m=0}^{n} K_m \cos(m\phi_{ijkl}), \tag{6.7}$$

where the sum can contain up to 12 terms.

Commonly applied intermolecular forces terms are van der Waals forces described through a Lennard−Jones 12-6 potential[89]

$$V(r_{ij}) = 4\epsilon \left[\left(\frac{\sigma}{r_{ij}} \right)^{12} - \left(\frac{\sigma}{r_{ij}} \right)^{6} \right], \tag{6.8}$$

where ϵ is the depth of the potential well, and σ is related to the equilibrium distance between the atoms. The parameters are usually obtained through fitting to experimental data and/or theoretical considerations.

6.1. *Subcellular element model*

In the subcellular element model (SEM),[108,8,135] each cell is modeled using a collection of soft particles. These subcellular elements (SCE) can be seen as a coarse-grained representation of a cell's cytoskeleton.

Following Sandersius *et al.*,[135] we employ a variation of the empirical morse potential which has been used before for bonds in polymers.[121,33] The interaction potential between two SCEs i and j is given by:

$$\phi(r_{ij}) = u_0 e^{2\rho\left(1-\frac{r^2}{r_{\text{eq}}^2}\right)} - 2u_0 e^{\rho\left(1-\frac{r^2}{r_{\text{eq}}^2}\right)}, \tag{6.9}$$

where u_0 is the potential well depth, ρ is a scaling factor, and r_{eq} is the equilibrium distance between two SCEs.

In the original formulation of the SEM,[108] Newman suggests to solve the equations of motion for the SCEs using the Brownian dynamics formulation which is a simplified version of Langevin dynamics. The Langevin formulation for the motion of a SCE i is:

$$m\ddot{r}_i = \xi - \eta\dot{r}_i - \sum_{i \neq j} F^C(r_{ij}), \tag{6.10}$$

where ξ represent thermal fluctuations and random polymerization and depolymerization events, η is the viscous drag coefficient and $F^C(r_{ij})$ the pairwise force on a

single SCE from neighboring ones. Since the environment of a cell is highly viscous, we can assume overdamped motion. There, we have $m\ddot{r}_i \ll \eta\dot{r}_i$ and we get Brownian dynamics by rearranging (6.10) and setting $m\ddot{r}_i = 0$:

$$\eta\dot{r}_i = \xi - \sum_{i \neq j} F^C(r_{ij}). \tag{6.11}$$

The resulting Eq. (6.11) is then solved using a stochastic integration scheme.

Sandersius *et al.*[135] conducted Brownian dynamics simulations to measure the viscoelasticity of the cell under axial compression between parallel plates, showing good qualitative agreement with experiments.[18,100,47,159] They also measured the shear storage and loss moduli (G', G'') in order to quantify the microrheology of their setup.

The SEM can be extended to model preferential cell adhesion and different cell compartments by changing the parameters of the potential in Eq. (6.9). Cell adhesion for instance is modeled by changing the relative strength of the inter- and intra-cellular potential wells, that is specifying different u_0^{inter} and u_0^{intra}. The boundary elements of a cell can be recognized and handled differently to model effects of surface tension or stiffer materials like the cell walls surrounding plant cells. Figure 16 shows a proliferating plant tissue where wall elements are automatically recognized and treated as a stiffer and stickier material. Wall elements can be connected to a neighboring cell such that the cells do not slide past each other. The boundary of the tissue grows with the enclosed cells and is modeled to have the same effect as if there were elements of a different cell all around it. Cells grow by adding new particles and thus mass in the center. As soon as a cell reaches a certain mass, it will divide with a division plane given by empirical rules. In Fig. 15 we show an extension of the SEM for cell migration where elements are added and removed to explicitly model polymerization and depolymerization events. The SEM also allows us to determine neighborhood relationships between cells and the size of their contact area. This can in turn be used to model juxtacrine signaling like in the Delta−Notch system[39] and provide a patterning mechanism while the cells evolve (see Fig. 17).

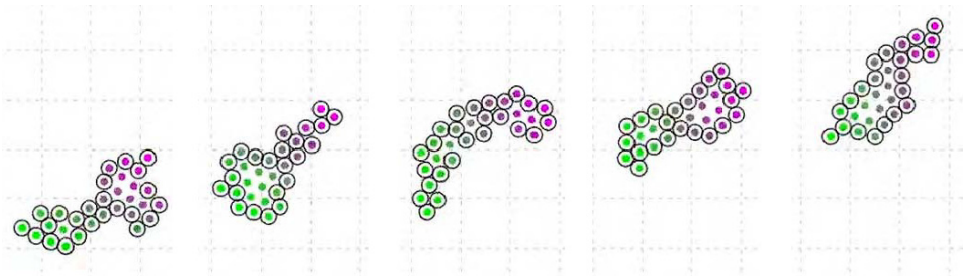

Fig. 15. Elements can be added and removed to model polymerization and depolymerization during cell migration.

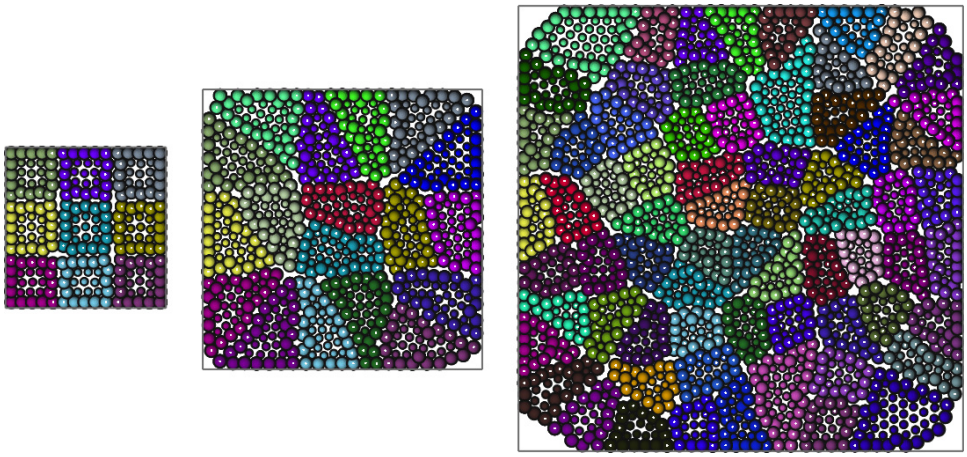

Fig. 16. A proliferating plant tissue with wall elements displayed as slightly larger spheres. The boundary of the tissue is shown as a gray box.

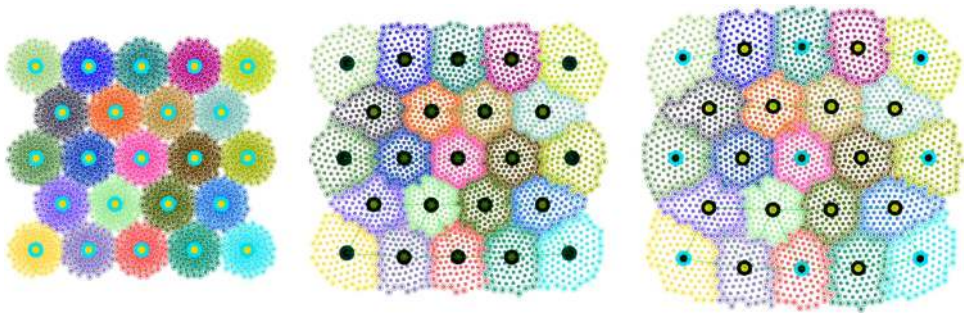

Fig. 17. Juxtacrine signaling can be applied on cells represented by SCEs while they evolve. The circle in the center of each cell represents the Notch-concentration (black is high, cyan is low) which determines the cell fate.

7. Conclusions

We have reviewed our recent efforts in developing particle methods for the simulation of morphogenesis, with examples in applications ranging from pattern formation to avascular tumor growth and sprouting angiogenesis. We have demonstrated that particle methods provide a flexible computational tool that can handle deterministic as well as stochastic models and the spatial and temporal complexity involved in morphogenesis. Current efforts focus on developing multiresolution stochastic[19] and deterministic[26] particle methods and their implementation in modern computer architectures.[129,138]

We wish to emphasize that the methods presented in this review are only a subset of the wealth available in particle based simulations for biological systems and morphogenesis. Notable omissions, include Potts models[68] and Cellular Autiomata[7]

that have been used extensively in studies related to developmental biology and morphogenesis (see Ref. 99 and references therein) and Dissipative Particle Dynamics.[78] In addition we wish to highlight the value and efforts of colleagues of the open source software for biological morphogenesis that is largely based on particle based methods: two examples are CompuCell 3D[2,139] and the Virtual Cell[4,67] (a non-exhaustive list of related software can be found at http://systems-biology.org/software). Last but not least we wish to mention the ongoing development of multiscale computational methods that mirror the very essence of morphogenesis by deriving systematically models in a hierarchical fashion starting from particle based descriptions (see Refs. 22, 30, 106 and references therein).

We close by emphasizing that the tools presented herein present only a first step in the direction of developing computational tools that will model effectively (i.e. with predictive capability) morphogenesis. Morphogenesis involves multiscale phenomena[52] and it is important to develop algorithms that can couple models ranging from the cellular (such as subcellular elements) to the tissue level such as particle level sets and their hierarchical interactions as well as their interactions with their microenvironment. We need to integrate mechanics with chemistry, feedback control and regulation mechanisms active across multiple temporal and spatial scales, signaling and tissue dynamics while taking advantage of developments in imaging and bioinformatics that continue to provide us with insight into the workings of the biological systems. We believe that these phenomena require models that go beyond the reaction−diffusion paradigm and require that experimental knowledge be translated into models for which we may not even have the necessary computational tools. While this provides an excellent arena for developing the next generation of computational methods, it also suggests the need of enhancing the dialog between biologists and computational scientists. This dialog is necessary so that the computational tools that are being developed are effective in answering biological problems and at the same time developing common scientific frontiers between modelers and experimentalists that can be effectively reached by joining forces.

Acknowledgments

We wish to acknowledge Dr. Michael Bergdorf who has laid the foundation of our work in this field. The simulations presented herein have benefitted from the work and software developments of Dr. Diego Rossinelli.

References

1. Brainweb: Simulated brain database. http://mouldy.bic.mni.mcgill.ca/brainweb.
2. Compucell. http://www.compucell3d.org.
3. Mayo clinic. http://www.mayoclinic.org/glioma/glioblastoma.html.
4. Virtual cell. http://www.vcell.org.
5. D. Adalsteinsson and J. A. Sethian, Transport and diffusion of material quantities on propagating interfaces via level set methods, *J. Comput. Phys.* **185** (2003) 271−288.

March 15, 2011 6:55:36pm WSPC/103-M3AS 00543 ISSN: 0218-2025 1st Reading

6. T. Aegerter-Wilmsen, A. C. Smith, A. J. Christen, C. M. Aegerter, E. Hafen and K. Basler, Exploring the effects of mechanical feedback on epithelial topology, *Development* **137** (2010) 499−506.
7. T. Alarcon, H. M. Byrne and P. K. Maini, A cellular automaton model for tumour growth in inhomogeneous environment, *J. Theor. Biol.* **225** (2003) 257−274.
8. W. Alt, F. Adler, M. Chaplain, A. Deutsch, A. Dress, D. Krakauer, R. T. Tranquillo, A. R. A. Anderson, M. A. J. Chaplain, K. A. Rejniak and T. Newman, Modeling multicellular structures using the subcellular element model, in *Single-Cell-Based Models in Biology and Medicine* (Birkhäuser, 2007), pp. 221−239.
9. A. R. A. Anderson, A hybrid mathematical model of solid tumour invasion: The importance of cell adhesion, *Math. Med. Biol.* **22** (2005) 163−186.
10. A. R. A. Anderson and M. A. J. Chaplain, Continuous and discrete mathematical models of tumor-induced angiogenesis, *Bull. Math. Biol.* **60** (1998) 857−900.
11. A. R. A. Anderson, M. A. J. Chaplain and K. A. Rejniak, *Single Cell Based Models in Biology and Medicine* (Birkhäuser, 2007).
12. N. J. Armstrong, K. J. Painter and J. A. Sherratt, A continuum approach to modelling cell−cell adhesion, *J. Theor. Biol.* **243** (2006) 98−113.
13. A. Auger, P. Chatelain and P. Koumoutsakos, R-leaping: Accelerating the stochastic simulation algorithm by reaction leaps, *J. Chem. Phys.* **125** (2006) 084103.
14. H. Axelson, E. Fredlund, M. Ovenberger, G. Landberg and S. Pahlman, Hypoxia-induced dedifferentiation of tumor cells — a mechanism behind heterogeneity and aggressiveness of solid tumors; Biology of hypoxia and myogenesis and muscle disease, *Sem. Cell & Developmental Biol.* **16** (2005) 554−563.
15. R. A. Bagnold, *Physics of Blown Sand and Desert Dunes* (Methuen, 1941).
16. R. Baker and P. Maini, A mechanism for morphogen-controlled domain growth, *J. Math. Biol.* **54** (2007) 597−622.
17. A. L. Bauer, T. L. Jackson and Y. Jiang, A cell-based model exhibiting branching and anastomosis during tumor-induced angiogenesis, *Biophys. J.* **92** (2007) 3105−3121.
18. A. R. Bausch, W. Moller and E. Sackmann, Measurement of local viscoelasticity and forces in living cells by magnetic tweezers, *Biophys. J.* **76** (1999) 573−579.
19. B. Bayati, P. Chatelain and P. Koumoutsakos, Adaptive mesh refinement for stochastic reaction−diffusion processes, *J. Comput. Phys.* **230** (2011) 13−26.
20. J. T. Beale, A convergent 3-D vortex method with grid-free stretching, *Math. Comput.* **46** (1986) 401−424.
21. E. L. Bearer, J. S. Lowengrub, H. B. Frieboes, Y.-L. Chuang, F. Jin, S. M. Wise, M. Ferrari, D. B. Agus and V. Cristini, Multiparameter computational modeling of tumor invasion, *Cancer Res.* **69** (2009) 4493−4501.
22. N. Bellomo, *Modeling Complex Living Systems — Kinetic Theory and Stochastic Game Approach* (Birkhäuser, 2008).
23. N. Bellomo, A. Bellouquid, J. Nieto and J. Soler, Multicellular biological growing systems: Hyperbolic limits towards macroscopic description, *Math. Models Methods Appl. Sci.* **17** (2007) 1675−1692.
24. ———, Multiscale biological tissue models and flux-limited chemotaxis for multicellular growing systems, *Math. Models Methods Appl. Sci.* **20** (2010) 1179−1207.
25. M. Bergdorf, Multireslution particle methods for the simulation of growth and flow, Ph.D. thesis, ETH Zurich, 2007.
26. M. Bergdorf and P. Koumoutsakos, A Lagrangian particle-wavelet method, *Multiscale Model. Simul.* **5** (2006) 980−995.
27. M. Bergdorf, I. Sbalzarini and P. Koumoutsakos, A Lagrangian particle method for reaction−diffusion systems on deforming surfaces, *J. Math. Biol.* **61** (2010) 649−663.

28. D. Bernstein, Simulating mesoscopic reaction−diffusion systems using the gillespie algorithm, *Phys. Rev. E* **71** (2005) 041103.
29. M. Bertalmio, L.-T. Cheng, S. Osher and G. Sapiro, Variational problems and partial differential equations on implicit surfaces, *J. Comput. Phys.* **174** (2001) 759−780.
30. C. Bianca and N. Bellomo, *Towards a Mathematical Theory of Complex Biological Systems*, Series in Mathematical Biology and Medicine (World Scientific, 2011).
31. H. Byrne and D. Drasdo, Individual-based and continuum models of growing cell populations: A comparison, *J. Math. Biol.* **58** (2009) 657−687.
32. Y. Cao, D. T. Gillespie and L. R. Petzold, Efficient step size selection for the tau-leaping simulation method, *J. Chem. Phys.* **124** (2006) 044109.
33. J. J. L. Cascales and J. G. de la Torre, Simulation of polymer chains in elongational flow, steady-state properties and chain fracture, *J. Chem. Phys.* **95** (1991) 9384−9392.
34. M. A. Chaplain, Mathematical modelling of angiogenesis, *J. Neurooncol.* **50** (2000) 37−51.
35. M. A. J. Chaplain, M. Ganesh and I. G. Graham, Spatio-temporal pattern formation on spherical surfaces: Numerical simulation and application to solid tumour growth, *J. Math. Biol.* **42** (2001) 387−423.
36. S. Chen, B. Merriman, S. Osher and P. Smereka, A simple level set method for solving stefan problems, *J. Comput. Phys.* **135** (1997) 8−29.
37. S. Christley, B. Lee, X. Dai and Q. Nie, Integrative multicellular biological modeling: A case study of 3D epidermal development using gpu algorithms, *BMC Syst. Biol.* **4** (2010) 107.
38. T. Cickovski, K. Aras, M. S. Alber, J. A. Izaguirre, M. Swat, J. A. Glazier, R. M. H. Merks, T. Glimm, H. G. E. Hentschel and S. A. Newman, From genes to organisms via the cell — A problem-solving environment for multicellular development, *Comput. Sci. Eng.* **9** (2007) 50−60.
39. J. R. Collier, N. A. M. Monk, P. K. Maini and J. H. Lewis, Pattern formation by lateral inhibition with feedback: A mathematical model of delta-notch intercellular signalling, *J. Theor. Biol.* **183** (1996) 429−446.
40. G.-H. Cottet, P. Koumoutsakos and M. L. Ould Salihi, Vortex methods with spatially varying cores, *J. Comput. Phys.* **162** (2000) 164−185.
41. G.-H. Cottet and P. D. Koumoutsakos, *Vortex Methods: Theory and Practice*, (Cambridge Univ. Press, 2000).
42. V. Cristini, J. Blawzdziewicz and M. Loewenberg, An adaptive mesh algorithm for evolving surfaces: Simulations of drop breakup and coalescence, *J. Comput. Phys.* **168** (2001) 445−463.
43. J. A. Davies, *Mechanisms of Morphogenesis* (Elsevier, 2005).
44. G. E. Davis and D. R. Senger, Endothelial extracellular matrix: Biosynthesis, remodeling, and functions during vascular morphogenesis and neovessel stabilization, *Circulation Res.* **97** (2005) 1093−1107.
45. P. Degond and S. Mas-Gallic, The weighted particle method for convection−diffusion equations. Part 1: The case of an isotropic viscosity, *Math. Comput.* **53** (1989) 485−507.
46. ———, The weighted particle method for convection−diffusion equations. Part 2: The anisotropic case, *Math. Comput.* **53** (1989) 509−525. Oct.
47. N. Desprat, A. Richert, J. Simeon and A. Asnacios, Creep function of a single living cell, *Biophys. J.* **88** (2005) 2224−2233.
48. O. Diekmann, R. Durrett, K. Hadeler, P. Maini and H. Smith, Mathematical models in morphogenesis, in *Mathematics Inspired by Biology*, Vol. 1714 (Springer, 1999), pp. 151−189.
49. D. Drasdo, R. Kree and J. S. McCaskill, Monte Carlo approach to tissue-cell populations, *Phys. Rev. E* **52** (1995) 6635−6657.

50. J. D. Eldredge, A. Leonard and T. Colonius, A general determistic treatment of derivatives in particle methods, *J. Comput. Phys.* **180** (2002) 686−709.
51. J. Elf and M. Ehrenberg, Spontaneous seperation of bi-stable biochemical systems into spatial domains of opposite phases, *Syst. Biol.* **1** (2004) 230−235.
52. A. J. Engler, P. O. Humbert, B. Wehrle-Haller and V. M. Weaver, Multiscale modeling of form and function, *Science* **324** (2009) 208−212.
53. D. Enright, R. Fedkiw, J. Ferziger and I. Mitchell, A hybrid particle level set method for improved interface capturing, *J. Comput. Phys.* **183** (2002) 83−116.
54. E. Fermi, J. Pasta and S. Ulam, Studies in nonlinear problems, Los Alamos report LA-1940 (1955).
55. N. Ferrara, H.-P. Gerber and J. LeCouter, The biology of VEGF and its receptors, *Nature Med.* **9** (2003) 669−676.
56. J. Folkman, Angiogenesis, *Ann. Rev. Med.* **57** (2006) 1−18.
57. ———, Angiogenesis: An organizing principle for drug discovery? *Nature Rev. Drug Discovery* **6** (2007) 273−286.
58. H. B. Frieboes, F. Jin, Y. L. Chuang, S. M. Wise, J. S. Lowengrub and V. Cristini, Three-dimensional multispecies nonlinear tumor growth−II: Tumor invasion and angiogenesis, *J. Theor. Biol.* **264** (2010) 1254−1278.
59. P. Friedl and E. B. Bröcker, The biology of cell locomotion within three-dimensional extracellular matrix, *Cell. Mol. Life Sci.* **57** (2000) 41−64.
60. J. M. Garcia-Ruiz, E. Melero-Garcia and S. T. Hyde, Morphogenesis of self-assembled nanocrystalline materials of barium carbonate and silica, *Science* **323** (2009) 362−365.
61. H. Gerhardt, M. Golding, M. Fruttiger, C. Ruhrberg, A. Lundkvist, A. Abramsson, M. Jeltsch, C. Mitchell, K. Alitalo, D. Shima and C. Betsholtz, VEGF guides angiogenic sprouting utilizing endothelial tip cell filopodia, *J. Cell Biol.* **161** (2003) 1163−1177.
62. P. Ghysels, G. Samaey, B. Tijskens, P. Van Liedekerke, H. Ramon and D. Roose, Multi-scale simulation of plant tissue deformation using a model for individual cell mechanics, *Phys. Biol.* **6** (2009) 016009.
63. M. Gibson and J. Bruck, Efficient exact stochastic simulation of chemical systems with many species and many channels, *J. Phys. Chem. A* **104** (2000) 1876−1889.
64. D. T. Gillespie, General method for numerically simulating stochastic time evolution of coupled chemical-reactions, *J. Comput. Phys.* **22** (1976) 403−434.
65. ———, Exact stochastic simulation of coupled chemical reactions, *J. Phys. Chem.* **81** (1977) 2340−2361.
66. ———, Approximate accelerated stochastic simulation of chemically reacting systems, *J. Chem. Phys.* **115** (2001) 1716−1733.
67. J. A. Glazier and F. Graner, Simulation of the differential adhesion driven rearrangement of biological cells, *Phys. Rev. E* **47** (1993) 2128−2154.
68. F. Graner and J. A. Glazier, Simulation of biological cell sorting using a two-dimensional extended potts model, *Phys. Rev. Lett.* **69** (1992) 2013−2016.
69. L. Greengard and V. Rokhlin, A fast algorithm for particle simulations, *J. Comput. Phys.* **73** (1987) 325−348.
70. O. Hamant, M. G. Heisler, H. Jonsson, P. Krupinski, M. Uyttewaal, P. Bokov, F. Corson, P. Sahlin, A. Boudaoud, E. M. Meyerowitz, Y. Couder and J. Traas, Developmental patterning by mechanical signals in arabidopsis, *Science* **322** (2008) 1650−1655.
71. L. G. Harrison and M. Kolar, Coupling between reaction−diffusion prepattern and expressed morphogenesis, applied to desmids and dasyclads, *J. Theor. Biol.* **130** (1988) 493−515.
72. L. G. Harrison, S. Wehner and D. M. Holloway, Complex morphogenesis of surfaces: Theory and experiment on coupling of reaction−diffusion patterning to growth, *Faraday Discuss.* **120** (2001) 277−294.

73. J. Hattne, D. Fange and J. Elf, Stochastic reaction−diffusion simulation with mesord, *Bioinformatics* **21** (2005) 2923−2924.
74. J. V. Henderson and A. J. Venables, The dynamics of city formation, *Rev. Econ. Dynam.* **12** (2009) 233−254.
75. S. E. Hieber and P. Koumoutsakos, A Lagrangian particle level set method, *J. Comput. Phys.* **210** (2005) 342−367.
76. R. W. Hockney and J. W. Eastwood, *Computer Simulation Using Particles*, 2nd edn. (Institute of Physics, 1988).
77. D. M. Holloway and L. G. Harrison, Algal morphogenesis: Modelling interspecific variation in Micrasterias with reaction−diffusion patterned catalysis of cell surface growth, *Phil. Trans. R. Soc. Lond. B* **354** (1999) 417−433.
78. P. J. Hoogerbrugge and J. M. V. A. Koelman, Simulating microscopic hydrodynamics phenomena with dissipative particle dynamics, *Europhys. Lett.* **19** (1992) 155−160.
79. Y. Jamali, M. Azimi and M. R. K. Mofrad, A sub-cellular viscoelastic model for cell population mechanics, *PLoS ONE* **5** (2010) e12097−.
80. G.-S. Jiang and D. Peng, Weighted ENO schemes for Hamilton−Jacobi equations, *SIAM J. Sci. Comput.* **21** (2000) 2126−2143.
81. D. Juric and G. Tryggvason, A front-tracking method for dendritic solidification, *J. Comput. Phys.* **123** (1996) 127−148.
82. J. A. Kaandorp, P. M. A. Sloot, R. M. H. Merks, R. P. M. Bak, M. J. A. Vermeij and C. Maier, Morphogenesis of the branching reef coral madracis mirabilis, *Proc. R. Soc. B* **272** (2005) 127−133.
83. Y. Kawaguchi, A morphological study of the form of nature, *SIGGRAPH Comput. Graph.* **16** (1982) 223−232.
84. N. D. Kirkpatrick, S. Andreou, J. B. Hoying and U. Utzinger, Live imaging of collagen remodeling during angiogenesis, *Am. J. Physiol. Heart Circ. Physiol.* (2007) 01234.2006−.
85. A. J. Koch and H. Meinhardt, Biological pattern formation: From basic mechanisms to complex structures, *Rev. Mod. Phys.* **66** (1994) 1481−1507.
86. P. Koumoutsakos, Multiscale flow simulations using particles, *Annu. Rev. Fluid Mech.* **37** (2005) 457−487.
87. S. Lee, S. M. Jilani, G. V. Nikolova, D. Carpizo and M. L. Iruela-Arispe, Processing of VEGF-A by matrix metalloproteinases regulates bioavailability and vascular patterning in tumors, *J. Cell Biol.* **169** (2005) 681−691.
88. C. Lemerle, B. Di Ventura and L. Serrano, Space as the final frontier in stochastic simulations of biological systems, *FEBS Lett.* **579** (2005) 1789−1794.
89. J. E. Lennard-Jones and J. Corner, The calculation of surface tension from intermolecular forces, *Trans. Faraday Soc.* **36** (1940) 1156−1162.
90. A. Leonard, Review. Vortex methods for flow simulation, *J. Comput. Phys.* **37** (1980) 289−335.
91. H. A. Levine, B. D. Sleeman and M. Nilsen-Hamilton, Mathematical modeling of the onset of capillary formation initiating angiogenesis, *J. Math. Biol.* **42** (2001) 195−238.
92. K. Lindsay and R. Krasny, A particle method and adaptive treecode for vortex sheet motion in three-dimensional flow, *J. Comput. Phys.* **172** (2001) 879−907.
93. W. K. Liu, S. Jun and Y. F. Zhang, Reproducing kernel particle methods, *Internat. J. Numer. Meth. Fluids* **20** (1995) 1081−1106.
94. P. Macklin and J. Lowengrub, Evolving interfaces via gradients of geometry-dependent interior poisson problems: Application to tumor growth, *J. Comput. Phys.* **203** (2005) 191−220.

95. P. Macklin, S. McDougall, A. Anderson, M. Chaplain, V. Cristini and J. Lowengrub, Multiscale modelling and nonlinear simulation of vascular tumour growth, *J. Math. Biol.* **58** (2009) 765−798.
96. P. K. Maini, K. J. Painter and H. N. P. Chau, Spatial pattern formation in chemical and biological systems, *J. Chem. Soc. Faraday Trans.* **93** (1997) 3601−3610.
97. G. Marechal and J.-P. Ryckaert, Atomic versus molecular description of transport-properties in polyatomic fluids. n-butane as an illustration, *Chem. Phys. Lett.* **101** (1983) 548−554.
98. J. G. McGarry, J. Klein-Nulend, M. G. Mullender and P. J. Prendergast, A comparison of strain and fluid shear stress in stimulating bone cell responses — A computational and experimental study, *Faseb J.* **18** (2004) 482−+.
99. R. M. H. Merks and J. A. Glazier, A cell-centered approach to developmental biology, *Physica A* **352** (2005) 113−130.
100. A. Micoulet, J. P. Spatz and A. Ott, Mechanical response analysis and power generation by single-cell stretching, *Chem. Eur. J. Chem. Phys.* **6** (2005) 663−670.
101. F. Milde, M. Bergdorf and P. Koumoutsakos, A Hybrid model for three-dimensional simulations of sprouting angiogenesis, *Biophys. J.* **95** (2008) 3146−3160.
102. I. D. Mishev, Finite volume methods on Voronoi meshes, *Numer. Meth. Part. Differ. Equ.* **14** (1998) 193−212.
103. J. J. Monaghan, Smoothed particle hydrodynamics, *Rep. Prog. Phys.* **68** (2005) 1703−1759.
104. P. M. Morse, Diatomic molecules according to the wave mechanics. II. vibrational levels, *Phys. Rev.* **34** (1929) 57−64.
105. J. Murray, *Mathematical Biology: Spatial Models and Biomedical Applications* (Springer-Verlag, 2003).
106. T. Murtola, A. Bunker, I. Vattulainen, M. Deserno and M. Karttunen, Multiscale modeling of emergent materials: Biological and soft matter, *Phys. Chem. Chem. Phys.* **11** (2009) 1869−1892.
107. T. J. Newman, Modeling multicellular systems using subcellular elements, *Math. Biosci. Eng.* **2** (2005) 613−624.
108. T. J. Newman, S. A. N. Santiago Schnell, P. K. Maini and T. J. Newman, Grid-free models of multicellular systems, with an application to large-scale vortices accompanying primitive streak formation, in *Current Topics in Developmental Biology*, Multiscale Modeling of Developmental Systems, Vol. 81 (Academic Press, 2008), pp. 157−182.
109. J. T. Oden, A. Hawkins and S. Prudhomme, General diffuse-interface theories and an approach to predictive tumor growth modeling, *Math. Models Methods Appl. Sci.* **20** (2010) 477−517.
110. S. Osher and J. A. Sethian, Fronts propagating with curvature-dependent speed — Algorithms based on Hamilton−Jacobi formulations, *J.Comput. Phys.* **79** (1988) 12−49.
111. S. Osher and R. Fedkiw, *Level Set Methods and Dynamic Implicit Surfaces*, Applied Mathematical Sciences, Vol. 153 (Springer, 2003).
112. G. F. Oster, J. D. Murray and P. K. Maini, A model for chondrogenic condensations in the developing limb — The role of extracellular-matrix and cell tractions, *J. Embryol. Exp. Morphol.* **89** (1985) 93−112.
113. E. Palsson and H. G. Othmer, A model for individual and collective cell movement in dictyosteliumdiscoideum, *Proc. Natl. Acad. Sci. USA* **97** (2000) 10448−10453.
114. N. Paweletz and M. Knierim, Tumor-related angiogenesis, *Critical Rev. Oncol./Hematol.* **9** (1989) 197−242.
115. J. E. Pearson, Complex patterns in a simple system, *Science* **261** (1993) 189−192.

116. D. Peng, B. Merriman, S. Osher, H. Zhao and M. Kang, A PDE-based fast local level set method, *J. Comput. Phys.* **155** (1999) 410−438.
117. S. Pennacchietti, P. Michieli, M. Galluzzo, M. Mazzone, S. Giordano and P. M. Comoglio, Hypoxia promotes invasive growth by transcriptional activation of the met protooncogene, *Cancer Cell* **3** (2003) 347−361.
118. I. V. Pivkin and G. E. Karniadakis, Accurate coarse-grained modeling of red blood cells, *Phys. Rev. Lett.* **101** (2008) 118105.
119. M. Plank and B. Sleeman, Lattice and non-lattice models of tumour angiogenesis, *Bull. Math. Biol.* **66** (2004) 1785−1819.
120. Z. Poltorak, T. Cohen, R. Sivan, Y. Kandelis, G. Spira, I. Vlodavsky, E. Keshet and G. Neufeld, VEGF145, a secreted vascular endothelial growth factor isoform that binds to extracellular matrix, *J. Biol. Chem.* **272** (1997) 7151−7158.
121. R. Puthur and K. L. Sebastian, Theory of polymer breaking under tension, *Phys. Rev. B* **66** (2002) 024304.
122. J. Ranft, M. Basan, J. Elgeti, J.-F. Joanny, J. Prost and F. Jülicher, Fluidization of tissues by cell division and apoptosis, *Proc. Natl. Acad. Sci. USA* **107** (2010) 20863−20868.
123. P.-A. Raviart, Particle approximation of first order systems, *J. Comput. Math.* **4** (1986) 50−61.
124. K. A. Rejniak, An immersed boundary model of the formation and growth of solid tumors, MBI Technical Report 19, Mathematical Biosciences Institute, The Ohio State University, 2004.
125. K. A. Rejniak, An immersed boundary framework for modelling the growth of individual cells: An application to the early tumour development, *J. Theor. Biol.* **247** (2007) 186−204.
126. J. Rodriguez, J. Kaandorp, M. Dobrzynski and J. Blom, Spatial stochastic modelling of the phosphoenolpyruvate- dependent phosphotransferase (pts) pathway in escherichia coli, *Bioinformatics* **22** (2006) 1895−1901.
127. T. Roose, S. J. Chapman and P. K. Maini, Mathematical models of avascular tumor growth, *SIAM Rev.* **49** (2007) 179−208.
128. L. Rosenhead, The spread of vorticity in the wake behind a cylinder, *Proc. R. Soc. Lond. A* **127** (1930) 590−612.
129. D. Rossinelli, M. Bergdorf, G.-H. Cottet and P. Koumoutsakos, GPU accelerated simulations of bluff body flows using vortex particle methods, *J. Comput. Phys.* **229** (2010) 3316−3333.
130. D. Rossinelli, M. Bergdorf, B. Hejazialhosseini and P. Koumoutsakos, Wavelet based adaptive simulation of complex systems on multicore architectures, in *Parallel Numerical Algorithms* (Delft, 2009).
131. D. Rossinelli and P. Koumoutsakos, Vortex methods for incompressible flow simulations on the GPU, *The Visual Computer* **12** (2008).
132. C. Ruhrberg, H. Gerhardt, M. Golding, R. Watson, S. Ioannidou, H. Fujisawa, C. Betsholtz and D. T. Shima, Spatially restricted patterning cues provided by heparin-binding VEGF-A control blood vessel branching morphogenesis, *Genes Dev.* **16** (2002) 2684−2698.
133. S. J. Ruuth and B. Merriman, A simple embedding method for solving partial differential equations on surfaces, *J. Comput. Phys.* **227** (2008) 1943−1961.
134. J.-P. Ryckaert and A. Bellemans, Molecular dynamics of liquid n-butane near its boiling point, *Chem. Phys. Lett.* **30** (1975) 123−125.
135. S. A. Sandersius and T. J. Newman, Modeling cell rheology with the subcellular element model, *Phys. Biol.* **5** (2008) 015002.

136. I. F. Sbalzarini, A. Hayer, A. Helenius and P. Koumoutsakos, Simulations of (an) isotropic diffusion on curved biological surfaces, *Biophys. J.* **90** (2006) 878–885.
137. I. F. Sbalzarini, A. Mezzacasa, A. Helenius and P. Koumoutsakos, Effects of organelle shape on fluorescence recovery after photobleaching, *Biophys. J.* **89** (2005) 1482–1492.
138. I. F. Sbalzarini, J. H. Walther, M. Bergdorf, S. E. Hieber, E. M. Kotsalis and P. Koumoutsakos, PPM — A highly efficient parallel particle-mesh library, *J. Comput. Phys.* **215** (2006) 566–588.
139. J. C. Schaff, B. M. Slepchenko and L. M. Loew, Physiological modeling with the virtual cell framework, *Methods Enzymol.* **321** (2000) 1–23.
140. M. Scott, T. Hwa and B. Ingalls, Deterministic characterization of stochastic genetic circuits, *Proc. Natl. Acad. Sci. USA* **104** (2007) 7402–7407.
141. G. Serini, D. Valdembri and F. Bussolino, Integrins and angiogenesis: A sticky business, *Exp. Cell Res.* **312** (2006) 651–658.
142. J. A. Sethian, Fast marching methods, *SIAM Rev.* **41** (1999) 199–235.
143. J. A. Sethian, Evolution, implementation, and application of level set and fast marching methods for advancing fronts, *J. Comput. Phys.* **169** (2001) 503–555.
144. K. Sims, Particle animation and rendering using data parallel computation, *Comput. Graphics* **24** (1990) 405–413.
145. B. L. Smith and A. Glezer, The formation and evolution of synthetic jets, *Phys. Fluids* **10** (1998) 2281–2297.
146. H. A. Stone, A simple derivation of the time-dependent convective-diffusion equation for surfactant transport along a deforming interface, *Phys. Fluids A* **2** (1990) 111–112.
147. A. B. Stundzia and C. J. Lumsden, Stochastic simulation of coupled reaction–diffusion processes, *J. Comput. Phys.* **127** (1996) 196–207.
148. S. Sun, M. F. Wheeler, M. Obeyesekere and C. W. Patrick, Jr., A deterministic model of growth factor-induced angiogenesis, *Bull. Math. Biol.* **67** (2005) 313–337.
149. M. Sussman, P. Smereka and S. Osher, A level set approach for computing solutions to incompressible two-phase flow, *J. Comput. Phys.* **114** (1994) 146–159.
150. K. R. Swanson, E. C. Alvord and J. D. Murray, A quantitative model for differential motility of gliomas in grey and white matter, *Cell Proliferation* **33** (2000) 317–329.
151. R. Thom, *Mathematical Models of Morphogenesis* (Ellis Horwood Ltd., 1983).
152. D. W. Thompson, *On Growth and Form*, 2nd edn. (Cambridge Univ. Press, 1942).
153. D. P. Tolle and N. Le Novere, Particle-based stochastic simulation in systems biology, *Curr. Bioinf.* **1** (2006) 315–320.
154. A. M. Turing, The chemical basis of morphogenesis, *Philos. Trans. R. Soc. Lond. Ser. B* **237** (1952) 37–72.
155. S. O. Unverdi and G. Tryggvason, A front-tracking method for viscous, incompressible, multi-fluid flows, *J. Comput. Phys.* **100** (1992) 25–37.
156. P. Van Liedekerke, E. Tijskens, H. Ramon, P. Ghysels, G. Samaey and D. Roose, Particle-based model to simulate the micromechanics of biological cells, *Phys. Rev. E* **81** (2010) 061906.
157. C. Varea, J. L. Aragon and R. A. Barrio, Turing patterns on a sphere, *Phys. Rev. E* **60** (1999) 4588–4592.
158. T. Weinkauf and H. Theisel, Curvature measures of 3D vector fields and their applications, *J. WSCG* **10** (2002) 507–514.
159. F. Wottawah, S. Schinkinger, B. Lincoln, R. Ananthakrishnan, M. Romeyke, J. Guck and J. Käs, Optical rheology of biological cells, *Phys. Rev. Lett.* **94** (2005) 098103.
160. J.-J. Xu and H. Zhao, An Eulerian formulation for solving partial differential equations along a moving interface, *SIAM J. Sci. Comput.* **19** (2003) 573–594.